

FLUOROETHYLENE CARBONATE EFFECTS AS AN ELECTROLYTE ADDITIVE  
ON THE INITIAL CATHODE ELECTROLYTE INTERFACE

by  
Anthony Donakowski

© Copyright by Anthony Donakowski, 2022

All Rights Reserved

A thesis submitted to the Faculty and the Board of Trustees of the Colorado School of Mines in partial fulfillment of the requirements for the degree of Master of Science (Materials Science).

Golden, Colorado

Date \_\_\_\_\_

Signed: \_\_\_\_\_

Anthony Donakowski

Signed: \_\_\_\_\_

Dr. K. Xerxes Steirer  
Thesis Advisor

Golden, Colorado

Date \_\_\_\_\_

Signed: \_\_\_\_\_

Dr. Eric Toberer  
Associate Professor  
Director of Materials Science  
Department of Physics

## ABSTRACT

Lithium ion battery technology has revolutionized how and where we use energy. However, improvements are still needed to increase lifespan, safety, and energy density. Electrolyte additives can provide a safe and economical route towards fast charging applications for layered mixed transition metal oxides. One such system of interest is the LiNiMnCoO (NMC) cathode paired with a graphite anode and the standard ethylene carbonate:ethylmethylene carbonate (EC):(EMC) Gen2 electrolyte. Common electrolyte additives include fluoroethylene carbonate (FEC), vinylene carbonate (VC), and Lithium difluoro (oxalate) borate (LiDFOB). Each of which are meant to stabilize the electrolyte and electrode surfaces by several different mechanisms. FEC was chosen for this study due to it having been shown to suppress parasitic side reactions between the electrolyte and cathode by promoting the formation of a solid electrolyte interface layer (SEI). Specifically, the cathode electrolyte interface (CEI) has been shown to form  $\text{Li}_2\text{CO}_3$ , LiF, LiOH, and other hydrocarbon species. Furthermore, the decomposition products of FEC will react with these surface species to stabilize the CEI while the decomposition products of FEC, VC will suppress continuous electrolyte cathode reactions. FEC further promotes cell stability by scrubbing HF that may have formed from any moisture contamination in the electrolyte. The ideal CEI would be a uniform layer of ionically conducting material that is also electronically insulating. An ideal candidate for an economical process for uniform CEI formation is the promotion of LiF using FEC.

To understand the material level process in which the FEC concentration controls the growth rate of LiF and how LiF will promote cell stability, NMC cathodes were closely investigated using X-ray Photoelectron Spectroscopy (XPS), X-ray Diffraction (XRD), Electrical Impedance Spectroscopy (EIS), and Scanning Electron Microscopy (SEM). Adding 1-2% by volume of FEC to the standard Gen2 electrolyte recipe facilitated the

growth of LiF-rich CEI as shown by XPS. Moreover, the LiF layer created a measurable, polarizing effect between transition metal cations and the anion containing electrolyte. Although, the LiF-rich CEI reduced discharge capacity, the composition of the CEI was directly affect by the FEC concentration and  $\text{LiPF}_6$  electrolyte decomposition products decreased. Data suggests that adding 5% vol. and above caused the FEC to become a co-solvent and increases the charge transfer resistance of NMC cathode as shown by EIS. Any changes in performance that could be attributed to the structural change of the NMC or cation mixing were ruled out using XRD and SEM. The concentration of LiF within the CEI layer increased steadily from 10.74% to 42.05% for washed electrodes, while the LiF concentration for cycled electrodes remained above 30% for all except the 2% FEC concentration.

## TABLE OF CONTENTS

ABSTRACT . . . . .	iii
LIST OF FIGURES . . . . .	vii
LIST OF TABLES . . . . .	xii
LIST OF SYMBOLS . . . . .	xiii
LIST OF ABBREVIATIONS . . . . .	xiv
ACKNOWLEDGMENTS . . . . .	xv
DEDICATION . . . . .	xvi
CHAPTER 1 INTRODUCTION . . . . .	1
CHAPTER 2 BACKGROUND . . . . .	5
2.1 Research Objective . . . . .	5
2.2 LiNiMnCoO Cathode SEI Composition for Long Cycle Life Testing . . . . .	5
2.3 LiF Growth on Various Electrode Materials . . . . .	7
2.4 Effects of FEC and other Electrolyte Additives on Solvation Chemistry . . . . .	11
2.5 Engineered Growth of the SEI on Electrode Materials . . . . .	15
2.6 The Merits of the NMC + FEC System and Purpose of Study . . . . .	17
CHAPTER 3 METHODS . . . . .	19
3.1 Device Fabrication . . . . .	19
3.1.1 Electrolyte Preparation . . . . .	19
3.1.2 Electrode Fabrication . . . . .	20
3.2 Cycling and Electrochemical Impedance Spectroscopy . . . . .	20

3.3	X-ray Photoelectron Spectroscopy . . . . .	25
3.3.1	XPS Components and Hardware Theory . . . . .	25
3.3.2	Measurement and Analysis . . . . .	27
3.3.3	XPS Quantification . . . . .	29
3.4	X-ray Diffraction . . . . .	31
3.5	Scanning Electron Microscope . . . . .	32
CHAPTER 4 INVESTIGATING THE CONTRIBUTION OF FLUOROETHYLENE CARBONATE TO CELL STABILITY IN LINI0.6MN0.6CO0.2O CATHODE CONTAIN LI-ION BATTERIES . . .		33
4.1	Focused Introduction . . . . .	33
4.2	Results . . . . .	35
4.2.1	Device Cycling and Electrochemical Impedance Spectroscopy . . . . .	35
4.2.2	Scanning Electron Microscopy and X-ray Diffraction . . . . .	39
4.2.3	X-ray Photoelectron Spectroscopy . . . . .	42
4.3	Discussion . . . . .	53
4.3.1	FEC Effects on Electrochemical Performance . . . . .	53
4.3.2	Surface Morphology and Structure of NMC Cathodes . . . . .	54
4.3.3	Chemical State of the SEI and Polarizing Effects due to Electrolyte Decomposition . . . . .	55
CHAPTER 5 CONCLUSION . . . . .		59
5.1	General Summary . . . . .	59
5.2	Outlook . . . . .	60
REFERENCES . . . . .		62
APPENDIX COPYRIGHT AND PERMISSIONS . . . . .		69

## LIST OF FIGURES

- Figure 1.1 Simple schematic of a Li- ion battery. From left to right the schematic displays the stainless steel coin cell case in black, the Al- current collector in light grey, the NMC cathode material in dark gray, and the LiF rich SEI in yellow. The center of the diagram depicts an enlarged space for the electrolyte where the electrolyte salt  $\text{LiPF}_6$  separates into Li and  $\text{PF}_6$  while Li ions travel to the cathode.  $\text{Ni}^{2+}$  dissolution along with  $\text{Li}_2$  metal plating are depicted as major causes of battery failure. The anode half of the schematic begins with the metal dendrites in light blue, followed by the graphite in light grey, Cu current collector in orange, and the other end of the stainless steel case in blue. . . . . 2
- Figure 2.1 Panel A shows voltage vs specific discharge capacity plots NMC811/graphite full cells cycled at 4.2 V, 4.4 V and 4.5V charged at C/2 rate and discharge at 1C rate. The 1st, 333rd, 667th, and 1000th cycles are plotted for cells at 25C. Panel B shows the capacity retention of the same cells and C the Coulombic efficiency. Reproduced with permission from Wangda Li, Xiaoming Liu, Qiang Xie, Ya You, Miaofang Chi, and Arumugam Manthiram. Long-term cyclability of ncm-811 at high voltages in lithium-ion batteries: an in-depth diagnostic study. *Chemistry of Materials*, 32(18):7796–7804, Sep 2020. ISSN 0897-4756, 1520-5002. doi: 10.1021/acs.chemmater.0c02398. . . . . 6
- Figure 2.2 XPS spectra of NMC electrodes from NMC811 graphite cells cycled at 4.2 V, 4.4 V and 4.5V charged at C/2 rate and discharge at 1C rate after 1000 cycles. A is the C 1s region showing the C-C, C-H, C-O, C=O, C-F, and  $\text{CF}_x$ . The O 1s region in panel B shows NiO standard along with M-O, O=C, and O-C bonds. Panel C is the F 1s core level with LiF/ $\text{MF}_x$ ,  $\text{Li}_x\text{POF}_y$ , PVdF and  $\text{CF}_x$ . Reproduced with permission from Wangda Li, Xiaoming Liu, Qiang Xie, Ya You, Miaofang Chi, and Arumugam Manthiram. Long-term cyclability of ncm-811 at high voltages in lithium-ion batteries: an in-depth diagnostic study. *Chemistry of Materials*, 32(18):7796–7804, Sep 2020. ISSN 0897-4756, 1520-5002. doi: 10.1021/acs.chemmater.0c02398. . . . . 7

Figure 2.3	Schematic of Li dead layers on a Li-Metal Anode in FEC containing cells. Discharge Capacity retention for FEC containing cells compared to standard Gen2 electrolyte. Reproduced with permission from Seong-Jin Park, Jang-Yeon Hwang, Chong S. Yoon, Hun-Gi Jung, and Yang-Kook Sun. Stabilization of lithium-metal batteries based on the in situ formation of a stable solid electrolyte interphase layer. <i>ACS Applied Materials Interfaces</i> , 10(21):17985–17993, May 2018. ISSN 1944-8244. doi: 10.1021/acsami.8b04592. . . . .	8
Figure 2.4	XRD spectra and SEM images of NMC811 electrodes cycled at 4.2 V, 4.4 V and 4.5V charged at C/2 rate and discharge at 1C rate afer 1000 cycles. Reproduced with permission from Wangda Li, Xiaoming Liu, Qiang Xie, Ya You, Miaofang Chi, and Arumugam Manthiram. Long-term cyclability of ncm-811 at high voltages in lithium-ion batteries: an in-depth diagnostic study. <i>Chemistry of Materials</i> , 32(18):7796–7804, Sep 2020. ISSN 0897-4756, 1520-5002. doi: 10.1021/acs.chemmater.0c02398. . . . .	9
Figure 2.5	Schematic of the decomposition of FEC. ROLi interacts and leads to LiF formation along with $CO_2$ gas generation. Vinodkumar Etacheri, Ortal Haik, Yossi Goffer, Gregory A. Roberts, Ionel C. Stefan, Rainier Fasching, and Doron Aurbach. Effect of fluoroethylene carbonate (fec) on the performance and surface chemistry of si-nanowire li-ion battery anodes. <i>Langmuir</i> , 28(1):965–976, Jan 2012. ISSN 0743-7463. doi: 10.1021/la203712s. . . . .	14
Figure 3.1	From left to right and top to bottom: A Assorted ingredients for electrode preparation including NMC powder in the silver bag, carbon black Seuper-P, and PvDF binder in the white jars, B high speed mixer used to prepare electrode slurry, C inside of high speed mixer, D vacuum oven used to dry electrode at 105C . . . . .	20
Figure 3.2	From left to right and top to bottom: A blade coating machine used to coat 40 um thick electrodes, B dried electrode sheet punching, C representation of electrode blade coating, D electrode position choice for punch . . . . .	21
Figure 3.3	(a) shows the equivalent circuit model components and (b) the corresponding EIS response. The cell used in this sample set was cycled using an Arbin cycling cabinet at 4.2V and a C/20 charge rate for 2 cycles. Each cell was then measured near an OCV of 4.2V. . . . .	24

Figure 3.4	Schematic of the XPS showing the incident AL X-rays hitting a black oval sample. The liberated photoelectron path in dashed red follows through the path guided by the Focusing Lenses. The entrance slit of width $W$ allows the photoelectrons into the semi-hemispherical analyser. A negative voltage is placed at both R1 V1 and R2 V2 to select the electrons along R0 with the $\Delta R$ which is half the beam width. Reproduced with permission from J. Bass. "Sr Design Poster, X-ray Photoelectron Spectroscopy on Light Emitting Devices", <i>Department of Physics, Colorado School of Mines, Golden, CO, 2018.</i> . . .	28
Figure 4.1	(a) is the first formation cycle for 1%, 2%, 5%, 15%, and 30% FEC concentrations in blue, orange, green, red, and purple respectively showing a large discharge capacity distribution. (b) is the first formation cycles for the second set of cells which show a tighter capacity distribution. (c) is the second formation cycle for the first set of cells which show the same wide capacity range but also show increased capacity for all FEC concentrations. (d) is the second formation cycle for the second set of cells which shows the tightest capacity distribution and the highest overall capacity except for 5% concentration which failed (possibly due to excess water contamination)	37
Figure 4.2	EIS curves for 1%, 2%, 5%, 15%, and 30% FEC containing cells in blue, orange, green, red, and purple. Data has been presented as to highlight the initial wide semi-circles associated with the cathode SEI. The purple curve 30% FEC begins at $7 \Omega$ while the rest of the curves begin near $5 \Omega$ which can be attributed to noise in the measurement system. The characteristic semi-circles have uniquely elongated shapes and large Warburg impedance. . . . .	38
Figure 4.3	SEM images of fresh NMC electrode depicting particles of various sizes. (A) NMC particle distribution in the binder material, 10 $\mu\text{m}$ scale at 6500x magnification gathered at 5keV. (B) 3 $\mu\text{m}$ scale at 20000x magnification at 5kV electron excitation voltage. (C) SEM image of cycled electrode in 2% FEC showing minor particle pulverization 10 $\mu\text{m}$ scale at 7000x magnification. (D) cycled electrode in 2% FEC 3 $\mu\text{m}$ scale at 20500x magnification at 5kV electron excitation voltage. (E) SEM image of cycled electrode in 15% FEC showing minor particle pulverization 10 $\mu\text{m}$ scale at 7000x magnification. (F) cycled electrode in 15% FEC 3 $\mu\text{m}$ scale at 20500x magnification at 5kV electron excitation voltage. Light gray portions are NMC particles while darker gray and black portions are binder material and carbon black. . . . .	40

Figure 4.4	XRD spectra normalized to the (003) peak to be 1. Spectra plotted for each FEC concentration 1%, 2%, 5%, 15%, and 30% in blue, orange, green, red, and purple. Miller indices for identified peaks are shown above the corresponding diffraction peak. Dashed black lines indicated no significant peak position changes. Peak assignment fits with the well known layered $\text{Li}_x\text{MO}_2$ type of NMC structure, with a space group of R-3m. . . . .	41
Figure 4.5	XPS survey for Washed electrodes of varying FEC concentrations 0%, 1%, 2%, 5%, 15%, and 30% in blue, orange, green, red, purple, and brown. Surveys are plotted together to highlight peak centroid changes and overall intensity differences. Peaks are labeled with assigned core levels Ni/F, F, O, C, Mn, Al, Li, and Co. . . . .	43
Figure 4.6	XPS survey for cycled electrodes of varying FEC concentrations 1%, 2%, 5%, 15%, and 30% in blue, orange, green, red, and purple. Surveys are plotted together to highlight peak centroid changes and overall intensity differences. Peaks are labeled with assigned core levels Ni/F, F, O, C, Mn, Al, Li, and Co. . . . .	44
Figure 4.7	XPS spectra of F 1s core level gathered from 694-680 eV plotted on individual y-scales. (a) is a washed electrode with 1% FEC concentration with LiF peak in orange and binder + electrolyte decomposition peak in green as is the same for all panels. (b) 2% FEC concentration, (c) 5% (d) 15%, (e) 30%. The right column contains (f) a cycled electrode for 1%FEC concentration followed by (g) 2%, (h) 5%, (i) 15%, and (j) 30% . . . . .	46
Figure 4.8	XPS spectra of C 1s core level gathered from 296-278 eV plotted on individual y-scales. (a) is a washed electrode with 1% FEC concentration with C-C peak in orange, H-C-O bond in green, C-O bond in orange, and C-F bond in brown as is the same for all panels. (b) 2% FEC concentration, (c) 5% (d) 15%, (e) 30%. The right column contains (f) a cycled electrode for 1%FEC concentration followed by (g) 2%, (h) 5%, (i) 15%, and (j) 30% . . . . .	47
Figure 4.9	XPS spectra of P 2p core level gathered from 143-124 eV plotted on individual y-scales. (a) is a washed electrode with 1% FEC concentration with $\text{Li}_x\text{PF}_y$ peak doublet in orange and green, $\text{Li}_x\text{PF}_y\text{O}_z$ peak doublet in red and purple, and $\text{Li}_w\text{-uPF}_z\text{-v}$ is the same for all panels. (b) 2% FEC concentration, (c) 5% (d) 15%, (e) 30%. The right column contains (f) a cycled electrode for 1%FEC concentration followed by (g) 2%, (h) 5%, (i) 15%, and (j) 30% . . . . .	48

Figure 4.10	XPS spectra of O 1s core level gathered from 543-524eV plotted on individual y-scales. (a) is a washed electrode with 1% FEC concentration with Li <sub>2</sub> CO <sub>3</sub> peak in orange, Li <sub>2</sub> CO <sub>3</sub> /Li <sub>x</sub> PF <sub>y</sub> O <sub>z</sub> in green, LiOH in red, and M-O bond in purple as is the same for all panels. (b) 2% FEC concentration, (c) 5% (d) 15%, (e) 30%. The right column contains (f) a cycled electrode for 1%FEC concentration followed by (g) 2%, (h) 5%, (i) 15%, and (j) 30% . . . . .	50
Figure 4.11	XPS centroid shifts plotted for 1%, 2%, 5%, 15%, and 30% FEC concentrations for both washed solid line and cycled electrodes dashed line. Centroids are plotted for F 1s, C 1s, O 1s, and P 2p core levels. . . . .	52
Figure 4.12	Schematic of the effect of FEC concentrations over 10% on solvation structure and SEI formation. EC is represented in blue shuttling orange Li ions in the SSIP configuration. The AGG configuration shows two Li cations and one PF <sub>6</sub> anion along with the formation of the SEI. . . . .	56
Figure 4.13	Resistance $\Omega$ versus LiF concentration using the peak area ratio of the LiF peak assignment in the XPS F 1s core level. Charge transfer resistance is displayed in blue and SEI resistance in orange. FEC concentrations are included as figure labels. Black lines pair the data sets and indicate differences in the resistance values . . . . .	57
Figure A.1	Copyright permission for Figure 2.1, Figure 2.2, and Figure 2.4 . . . . .	69
Figure A.2	Copyright permission for Li dead layer shown in Figure 2.3 . . . . .	70
Figure A.3	Copyright permission for FEC decomposition schematic Figure 2.5 . . . . .	70
Figure A.4	Copyright permission for XPS schematic in Figure 3.4 . . . . .	71

## LIST OF TABLES

Table 4.1	Resistance values for the Ohmic, SEI, and charge transfer components of the EIS curves. The capacitance of the SEI is also reported. All values are shown for 1%, 2%, 5%, 15%, and 30% FEC after the initial discharge cycles. . . . .	36
Table 4.2	Relative atomic concentrations calculated from F 1s, C 1s, O 1s, and P 2p for 1%, 2%, 5%, 15% and 30% FEC loading for both washed and cycled electrodes along with Gen2 control for the washed electrodes . . . . .	42
Table 4.3	Washed and Cycled electrode XPS core level peak area ratios. Percent form for Gen 2 and each FEC concentration 0%, 1%, 2%, 5%, 15%, and 30% broken between LiF and LiyPFx+PvDF components for F 1s, O-C-O, C-O, H-C-O, and C-F components for C 1s, LixPyFz and PvDF for P2p, and Li2CO3, LiOH, and M-O for O 1s. . . . .	51

## LIST OF SYMBOLS

Ionic Conductivity through an electrode surface . . . . .	$\mu$
Overpotential in the Butler-Volmer Equation . . . . .	$\eta$
Resistance in an electrochemical system . . . . .	R
Diffraction angle as determined by XRD . . . . .	$\theta$

## LIST OF ABBREVIATIONS

Binding Energy . . . . .	BE
Colorado School of Mines . . . . .	CSM
Counts per Second . . . . .	cps
Electric Vehicles . . . . .	EV
Energy Storage . . . . .	ES
Fluoroethylene Carbonate . . . . .	FEC
LiNiMnCoO . . . . .	NMC
Vinylene Carbonate . . . . .	VC

## ACKNOWLEDGMENTS

I would like to thank and acknowledge my advisor K. Xerxes Steirer for all his guidance and patience. I'd like to thank Shriram Santhanagopalan for sharing his wealth of experience and joining my committee. I would also like to thank my family for their unending support thorough my career. Thank you to my committee chair Stephen DeCaluwe for his guidance. This work would also not be possible without funding from the DOE Hi-Ni cathode research consortium.

I dedicate this thesis to my family.

# CHAPTER 1

## INTRODUCTION

Solving the challenges associated with energy storage will open the way for more renewable energy sources to be used. Li-ion battery have been the go to energy storage solution for many applications ranging from small electronics to electric vehicles and grid support [1]. More energy and power dense energy storage devices will reduce the need for fossil fuel consumption by storing the excess energy generated by renewable sources during non peak times. Extending the life of Li-ion batteries will allow this excess energy to be safely and efficiently distributed as electricity during peak hours. In conjunction with renewable sources like wind, tidal, and solar power, Li ion batteries have the potential to reduce greenhouse gas emissions and provide an economical route to energy security. Li-ion devices are lighter and have a longer cycle life than lead-acid equivalent [2]. Moreover, Li-ion batteries can maintain a constant voltage during discharge and have a longer shelf life [1–3].

The principle behind the operation of a Li-ion battery is the flux of  $\text{Li}^+$  ions from the cathode to the anode. As the ions flow though the device their electron pairs flow through an external circuit. To store energy by charging a Li-ion battery a potential difference is set across the device to flow current in the reverse direction. Li stored in the cathode material in the form of lithium metal oxides is freed and moves across a Li ion containing electrolyte solution. The Li then forms a chemical bond with the anode material. For example, a graphite anode Li reacts with the anode material to form  $\text{LiC}_6$  until the battery reaches the cell cutoff voltage. When a resistive load is placed across the battery the Li ions flow the other direction from anode to cathode and ideally reform the initial Li metal oxide material. The free electrons produced by the decomposition of  $\text{LiC}_6$  then produce electrical work through the external circuit as shown in Figure 1.1.

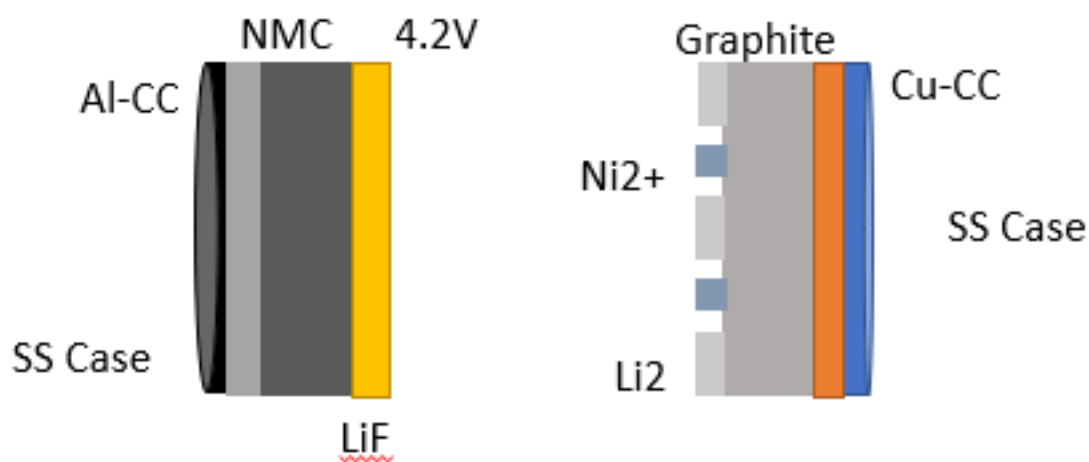


Figure 1.1 Simple schematic of a Li- ion battery. From left to right the schematic displays the stainless steel coin cell case in black, the Al- current collector in light grey, the NMC cathode material in dark gray, and the LiF rich SEI in yellow. The center of the diagram depicts an enlarged space for the electrolyte where the electrolyte salt LiPF<sub>6</sub> separates into Li and PF<sub>6</sub> while Li ions travel to the cathode. Ni<sup>2+</sup> dissolution along with Li<sub>2</sub> metal plating are depicted as major causes of battery failure. The anode half of the schematic begins with the metal dendrites in light blue, followed by the graphite in light grey, Cu current collector in orange, and the other end of the stainless steel case in blue.

The flow of Li ions is facilitated by the electrolyte. Common electrolyte solvents include ethylene carbonate (EC), ethylmethylene carbonate (EMC), and dimethylene carbonate (DMC) which provide good Li conductivity, low viscosity, and high electronic resistance. An ionic salt with low activation energy, like  $\text{LiPF}_6$ , is used as the electrolyte in several Li ion systems such as Si nano-wire [4], Li metal [5], and mixed transition metal oxides [6]. Under cycling conditions the electrolyte tends to degrade by oxidation of the salt which causes accumulation of decomposition products on the surface of the electrodes [7]. At worse case these decomposition products can cause an internal short and compromise the safe operation of Li-ion battery systems by leading to thermal runaway and fire [2]. More often these reaction products can reduce the discharge capacity and cycle life of the battery by consuming active material and degrading the electrolyte solvent and salt.

Mixed transition metal oxides like  $\text{LiCoO}$  (LCO),  $\text{LiNiCoO}$  (LNCO), and  $\text{LiNi}_x\text{Co}_y\text{Mn}_z\text{O}$  (NMCxyz) have demonstrated high safety and efficiency and are commercially available as cathode materials [8]. One of the current focuses in the development of Ni-rich cathodes is the support for fast charging applications at voltages above 4.2 V. Several strategies have been proposed to achieve higher charge rates including adding vinylene carbonate (VC) and fluoroethylene carbonate (FEC) to the standard Gen2 EC:EMC. The electrolyte composition plays a vital role in ensuring chemical stability, cycle retention, and stabilizing Coulombic efficiency with any cathode material. The decomposition of the electrolyte and formation of undesirable products has been found to be unavoidable in realistic manufacturing conditions [9]. Some species like LiF can be beneficial to battery performance by creating a barrier to prevent further reaction between the cathode and electrolyte. Other species including  $\text{Li}_x\text{PF}_y$  variants and HF are also produced after electrolyte degradation.  $\text{Li}_x\text{PF}_y$  and HF once produced can be difficult to eliminate, but fortunately the reaction forming  $\text{Li}_x\text{PF}_y$  is reversible during cycling [9]. HF is never consumed by the standard Li-ion chemistry and continues to react with the cathode, anode, electrolyte, current collectors, and stainless steel casing. The electrolyte

and the decomposition products may also further react with the binder material in the cathode as well as any residual surface contaminants including  $\text{Li}_2\text{CO}_3$ ,  $\text{LiOH}$ , and  $\text{H}_2\text{O}$  [9]. These parasitic surface reactions cause the loss of active material and can damage the structure of the NMC particle and crystal lattice [10]. The loss of active material and structural damage to the cathode is a detriment to device performance causing both voltage fade and capacity loss [9]. Li metal dendrites can also form and penetrate the cathode material making contact with the Al collector. The formation and contact of Li metal dendrites can cause internal short circuits which in turn cause the battery to fail and undergo thermal runaway potentially resulting in a fire [11].

The formation or deposition of a solid electrolyte interface (SEI) on one or both of the device electrodes has shown to increase the chemical and structural stability of the electrode surface [6]. The SEI on cathode is of particular interest because of the complex surface chemistry. The cathode electrolyte interface (CEI) is primarily composed of electrolyte decomposition products, solvent decomposition products, and other parasitic reactions with the NMC cathode and surface contaminants.  $\text{LiF}$ , one of the electrolyte decomposition products and a product of further parasitic reactions with  $\text{HF}$ , shows remarkable chemical stability with electrolyte solvents and the NMC cathode along with reasonable electronic insulation [9]. However,  $\text{LiF}$  has a lower Li ionic conductivity than NMC and other novel coatings including  $\text{Li}_3\text{PO}_4$  [12]. While the capacity of a Li ion battery with a  $\text{LiF}$  rich SEI may suffer, the economical benefits associated with the ease of device fabrication and increased cycle life outweighs a small loss in performance. Further investigation into the initial state of the SEI has not been reported as most studies characterize the electrode surfaces at the end of device life [13].

## CHAPTER 2

### BACKGROUND

#### 2.1 Research Objective

The objective of this review is to investigate the effects of electrolyte additives on the SEI formation and LiB performance. Specifically, the chemical stability of FEC with the Gen2 electrolyte and various cathode materials must be examined to understand the choice of additive.

#### 2.2 LiNiMnCoO Cathode SEI Composition for Long Cycle Life Testing

To model and characterize the SEI several Li-ion battery chemistries have been tested in the literature. A substantial portion focuses on the decomposition of the electrolyte. Specifically, the degradation mechanism of  $\text{LiPF}_6$  in Li/Li symmetric cells has been shown to create a dead Li layer on Li anodes followed by a LiF rich SEI [14]. Moreover, the mechanism for LiF growth on NMC has not been extensively studied. For example Park et al. showed that the fluorinated solvent EMC:FEC(3:1) reduces the thickness of the dead material compared to EC:EMC(3:7) solvents [15]. Adding the additive FEC to an EC based electrolyte will promote cell stability by encouraging the growth of a LiF rich CEI. Suo et al. proposed that a LiF rich CEI will reduce the discharge capacity but ultimately improve cycle life by limiting the degradation of  $\text{LiPF}_6$  [16].

The degradation of the electrolyte over long cycle lives at high voltages highlights the need for a stabilizing agent. Figure 2.1 and Figure 2.2 reproduced from Li et al. detail the formation of LiF at higher cutoff voltages but the overall shape and intensity of the PvDF and  $CF_x$  peaks do not change [10]. Moreover as voltage increases the capacity retention drastically decreases with cycle life. However, the Coulombic efficiency of all cases is above 99% but a clear downward trend is apparent for the higher cutoff voltages.

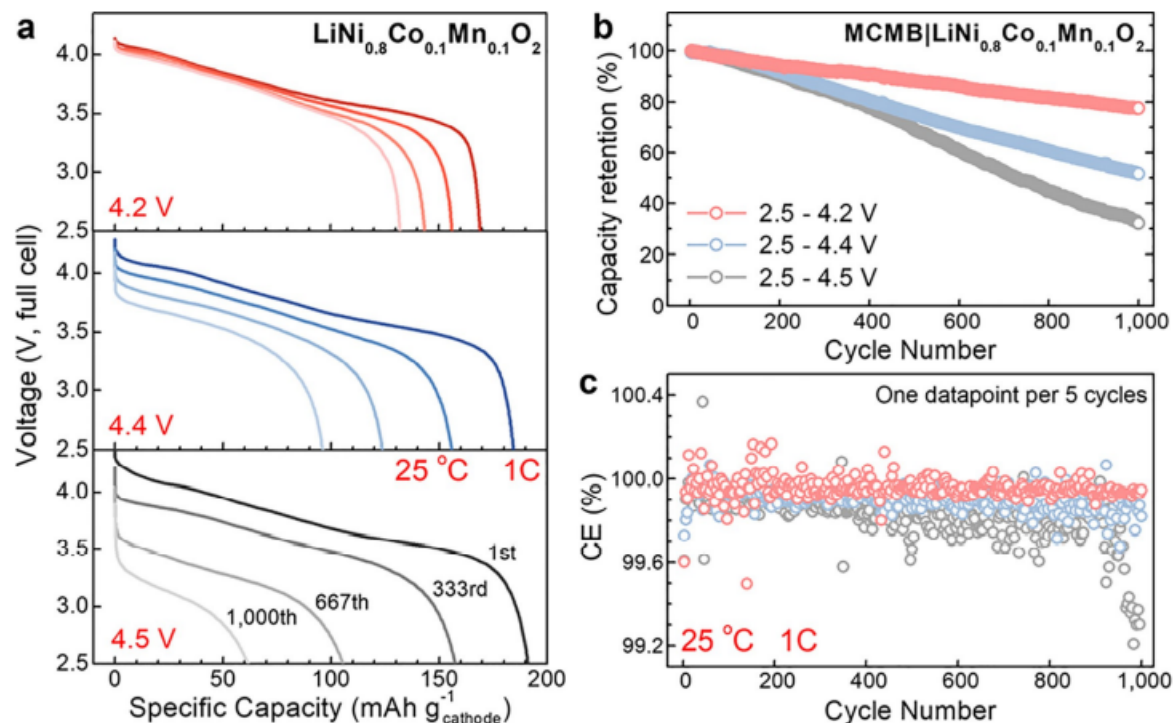


Figure 2.1 Panel A shows voltage vs specific discharge capacity plots NMC811/graphite full cells cycled at 4.2 V, 4.4 V and 4.5V charged at C/2 rate and discharge at 1C rate. The 1st, 333rd, 667th, and 1000th cycles are plotted for cells at 25C. Panel B shows the capacity retention of the same cells and C the Coulombic efficiency. Reproduced with permission from Wangda Li, Xiaoming Liu, Qiang Xie, Ya You, Miaofang Chi, and Arumugam Manthiram. Long-term cyclability of ncm-811 at high voltages in lithium-ion batteries: an in-depth diagnostic study. *Chemistry of Materials*, 32(18):7796–7804, Sep 2020. ISSN 0897-4756, 1520-5002. doi: 10.1021/acs.chemmater.0c02398.

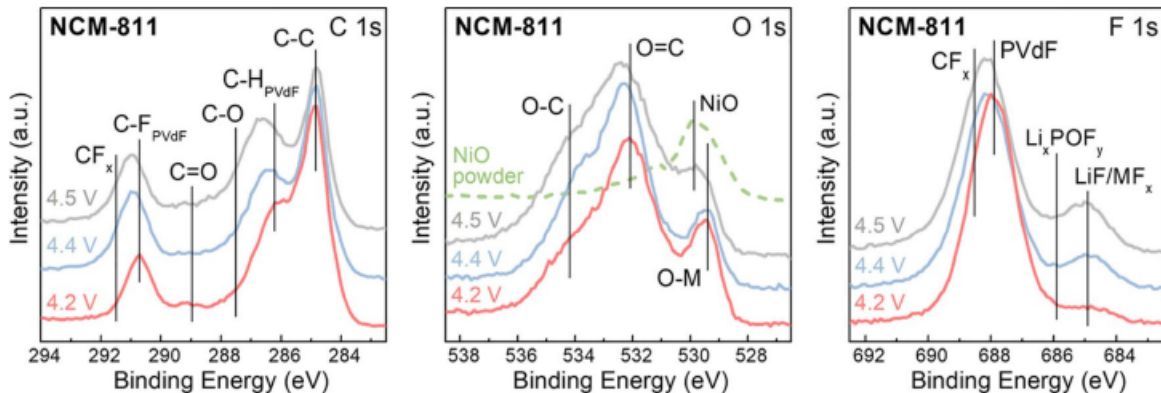


Figure 2.2 XPS spectra of NMC electrodes from NMC811 graphite cells cycled at 4.2 V, 4.4 V and 4.5V charged at C/2 rate and discharge at 1C rate after 1000 cycles. A is the C 1s region showing the C-C, C-H, C-O, C=O, C-F, and  $CF_x$ . The O 1s region in panel B shows NiO standard along with M-O, O=C, and O-C bonds. Panel C is the F 1s core level with  $LiF/MF_x$ ,  $Li_xPOF_y$ , PVdF and  $CF_x$ . Reproduced with permission from Wangda Li, Xiaoming Liu, Qiang Xie, Ya You, Miaofang Chi, and Arumugam Manthiram. Long-term cyclability of ncm-811 at high voltages in lithium-ion batteries: an in-depth diagnostic study. *Chemistry of Materials*, 32(18):7796–7804, Sep 2020. ISSN 0897-4756, 1520-5002. doi: 10.1021/acs.chemmater.0c02398.

The XPS spectra shown in Figure 2.2 show a measurable increase in LiF concentration as voltage increases. The LiF formation also appears to thicken with increased voltage as the metal-oxide (M-O) peak at 529 eV in the O 1s spectra becomes obscured. Moreover, the binder material appears to remain stable as the peak shape and position of the C-F bond at 291 eV do not drastically change with increasing voltage. One conclusion that can be drawn from these XPS results is that the LiF is primarily being formed from the electrochemical decomposition of the  $LiPF_6$  electrolyte. The PvdF binder does appear to break down and experience a change in the chemical state of the C-H bond at higher voltages when looking at the 286 eV peak in the C 1s spectrum of Figure 2.2.

### 2.3 LiF Growth on Various Electrode Materials

Figure 2.3 shows a schematic of the relevant growth of LiF on a Li metal anode and the resulting capacity loss seen in NMC/Li devices with a EC:EMC electrolyte solvent and a

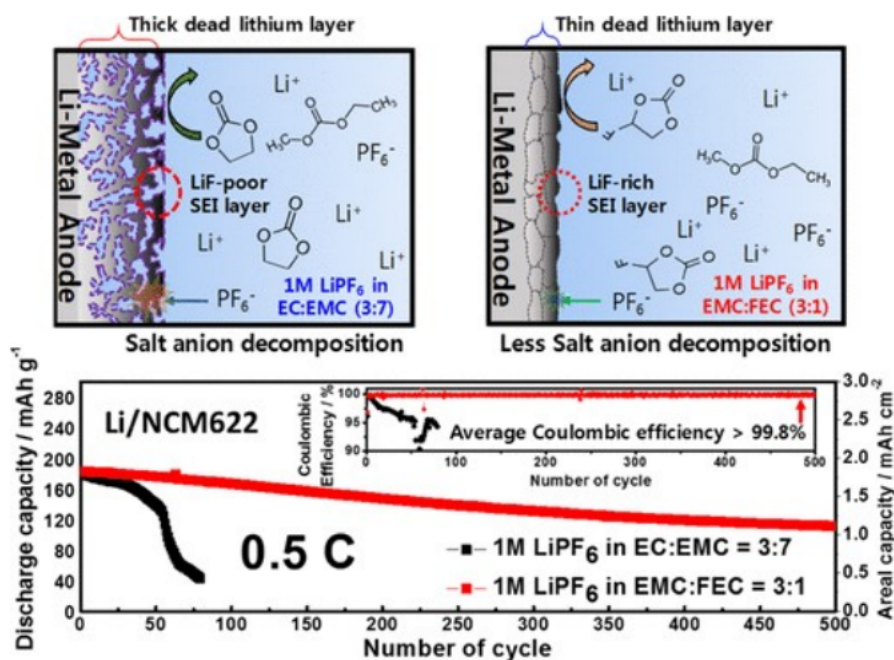


Figure 2.3 Schematic of Li dead layers on a Li-Metal Anode in FEC containing cells. Discharge Capacity retention for FEC containing cells compared to standard Gen2 electrolyte. Reproduced with permission from Seong-Jin Park, Jang-Yeon Hwang, Chong S. Yoon, Hun-Gi Jung, and Yang-Kook Sun. Stabilization of lithium-metal batteries based on the in situ formation of a stable solid electrolyte interphase layer. ACS Applied Materials Interfaces, 10(21):17985–17993, May 2018. ISSN 1944-8244. doi: 10.1021/acsami.8b04592.

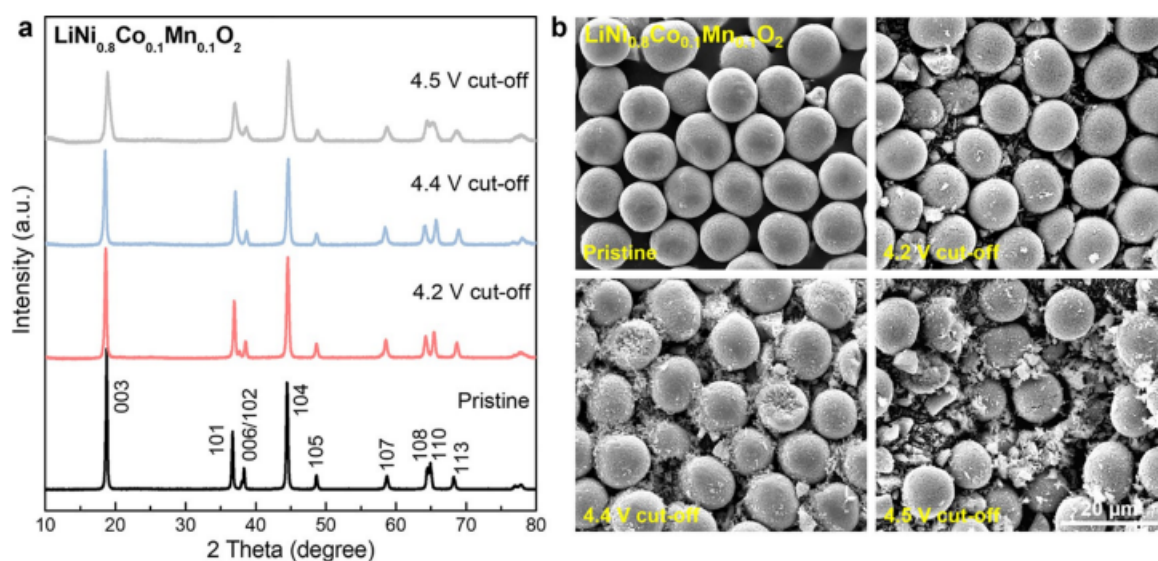


Figure 2.4 XRD spectra and SEM images of NMC811 electrodes cycled at 4.2 V, 4.4 V and 4.5V charged at C/2 rate and discharge at 1C rate after 1000 cycles. Reproduced with permission from Wangda Li, Xiaoming Liu, Qiang Xie, Ya You, Miaofang Chi, and Arumugam Manthiram. Long-term cyclability of ncm-811 at high voltages in lithium-ion batteries: an in-depth diagnostic study. *Chemistry of Materials*, 32(18):7796–7804, Sep 2020. ISSN 0897-4756, 1520-5002. doi: 10.1021/acs.chemmater.0c02398.

EMC:FEC solvent both with 1M  $LiPF_6$ . The EC:EMC system experiences the depletion of active material in the Li metal anode by delithiation and subsequent formation of electrolyte decomposition products. The EMC:FEC solution experienced a longer cycle life that is attributed to a LiF-rich SEI layer which prevented the  $PF_6$  anion from adsorbing into the Li metal anode. The FEC containing solution showed promising capacity retention and coulombic efficiency when compared to the EC:EMC solution [11].

Figure 2.4 shows XRD spectra and SEM images of NMC particles that have been cycled at high voltages. The XRD data along with the SEM images detail the gradually increasing mechanical pulverization of the NMC particles after cycling. The XRD spectra of the cycled peaks show shape changes including FWHM, intensity, and centroid position for the 003, 006/102, and 108/110 peak pairs. The SEM images provide insight into the surface roughness of the SEI as well as the order of the NMC particles. As voltage increases the NMC spheres break apart and void are formed in the binder material.

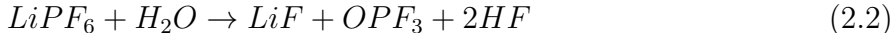
The interface between the NMC and the electrolyte must be stabilized to achieve higher energy density in Li-ion batteries [6]. Pham et al. have shown that a methoxytriethyleneoxypropyltrimethoxysilane (MTE-TMS) additive provides such increased stability that an NMC device capacity retention of 84% after 100 cycles at C/5 using upper voltage cut-off of 4.3 V vs Li+/Li [6]. Li et al. et al. have shown that triphenyl borate (TPB) as an additive forms a borate based CEI layer on an NMC cathode and the device had 88.6% capacity retention after 100 cycles [17]. Both of these studies provide a novel additive that increases NMC performance by forming an CEI layer. The mechanisms of how device performance is improved are also quite similar. The additive proposed by both decompose prior to the electrolyte solvents and oxidation of the electrolyte. The CEI is then composed of the decomposition products of the additive instead of the electrolyte solution.

## 2.4 Effects of FEC and other Electrolyte Additives on Solvation Chemistry

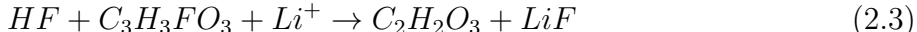
The motivation for choosing FEC as an electrolyte additive is the favourable reaction chemistry which enhances the lifetime of anode materials. However the affect of FEC on cathode materials is not as well understood. Li et al. have shown that FEC increases the oxidative stability of standard EC containing electrolytes as well as a preferential reaction at the cathode during charging [17]. Li et al attribute the increases stability to the suppression of parasitic reactions between the electrode and electrolyte by forming a conductive interfacial layer at the electrode surface. The hydrodefluorination of FEC into VC is the primary mechanism in which FEC affects the device performance [17]. Currently, the decomposition reaction:



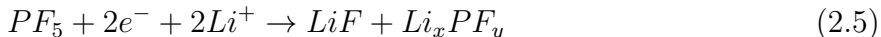
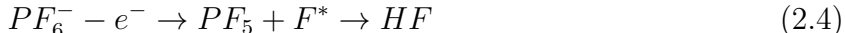
is reported in literature [7], but disputed by atomistic modeling groups [18]. The other decomposition reaction requires trace water



The appearance of HF then produces the desired reaction:



in which the initial HF is never consumed [8]. 2.3 shows free Li ions being consumed to form LiF; however, this is done without the defluorination of the PF<sub>6</sub> ion which prevents further electrolyte decomposition according to:



assuming all water is consumed in the decomposition of the electrolyte salt. Zhou et al. has shown LiNiMnO (LMNO) in addition to 4% FEC shows improved rate capacity and high temperature cycling performance [19]. Using Raman spectroscopy Zhou et al.

demonstrated that FEC increases the conductivity of the electrolyte[19]. FEC has also been studied in NMC/Li cells at high voltages. Instead of an electrolyte additive Lavi et al. achieved excellent performance by replacing EC by DEC and FEC[20]. LNMO/Li study results show that FEC can change the structure of aggregates (AGGs) in the electrolyte solution to the structure of solvent-separated ion pairs(SSIPs). Hou et al. detail the effects of the solvation structure on Li conductivity [21]. They propose that an anion-solvent exchange mechanism is the preferred method of transport of the Li ion while the preferential reduction of FEC forms an improved electrolyte interphase. Atomistic modeling using molecular dynamics and transport property measurements showed that the Gen2 electrolyte with 10% FEC passivates the electrode surface [21].

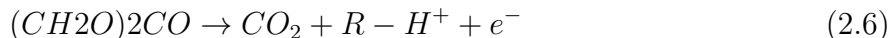
Zhou et al. also showed that concentrated electrolytes decrease solvent reduction, a LiF rich film forms and enhances interfacial stability [19]. The SEI conductivity on Li metal anodes [22] is also a good indicator of the capabilities of FEC as an electrolyte additive. Using large cylindrical cells (18650 model) at large concentrations of FEC have been found to enhance the transport property[23], while small amounts of FEC show that cycling performance and rate capability of NMC is improved by stabilizing the CEI [17]. Furthermore Yang et al. show that FEC concentrations greater than 5% reduces discharge capacity [24] and causes large concentration polarization [17]. Several papers report simulations that show FEC concentration directly determines the diffusion coefficients of Li+ and PF6-, but the effect of FEC on the CEI chemistry is not well understood. Some simulations suggest that FEC plays an active role in the defluorination of LiPF6 and fluorination of PF5 [25].

The main issue at the CEI is the loss of the active material Li2O which results in cation mixing at the surface that eventually penetrates the lattice[23]. The decomposition process of FEC proposed by Li et al. as seen in Figure 2.5 is supported by several XPS studies and DFT simulations [23, 26, 27]. FEC has been shown to reduce parasitic side reactions at the electrolyte/electrode interface at 1% and 2% concentrations by stabilizing the NMC surface

[23]. This is done at the cost of decomposing the electrolyte with FEC in the attempt to prevent further interaction with the NMC cathode[17]. At long cycle life FEC also suppressed changes in charge transfer resistance and the interfacial resistance of the CEI compared to standard Gen 2 recipes [17]. The cause of these increase resistances in batteries without FEC is due to the decomposition of the standard carbonate based electrolytes [28]. In addition FEC can slow the dissolution of Ni, Co, and Mn at the electrode surface and prevent the release of oxygen thereby maintaining the desirable electrochemical properties of NMC [20]. Improvements during the first few cycles of FEC containing devices show high coulombic efficiency by scavenging any HF that may have initially formed due to the presence of water [28].

Another electrolyte additive that has shown similar properties to FEC is the aforementioned VC [29]. Kitz et al. have shown that VC not FEC can suppress continuous side reaction at the CEI [29]. Again shown by DFT calculations [30], operando XPS studies [29] one of the decomposition products of FEC is VC, and the reduction of charge transport is attributed to VC [31]. Figure 2.5 shows the potential reaction pathway and the decomposition products of FEC and carbonate based electrolytes directly affect the CEI composition.

The prevention of the electrochemical oxidation of EC at high voltages



and the chemical oxidation by oxygen release [32]



by the dehydrofluorination of FEC shown in Figure 2.5



has been proposed as the main mechanism of CEI growth due to the addition of FEC. [33]. Markevich et al. found that the films formed on the surface of Sulfur/Carbon composite electrodes were primarily made of LiF crystallites using EDS and XPS [34].

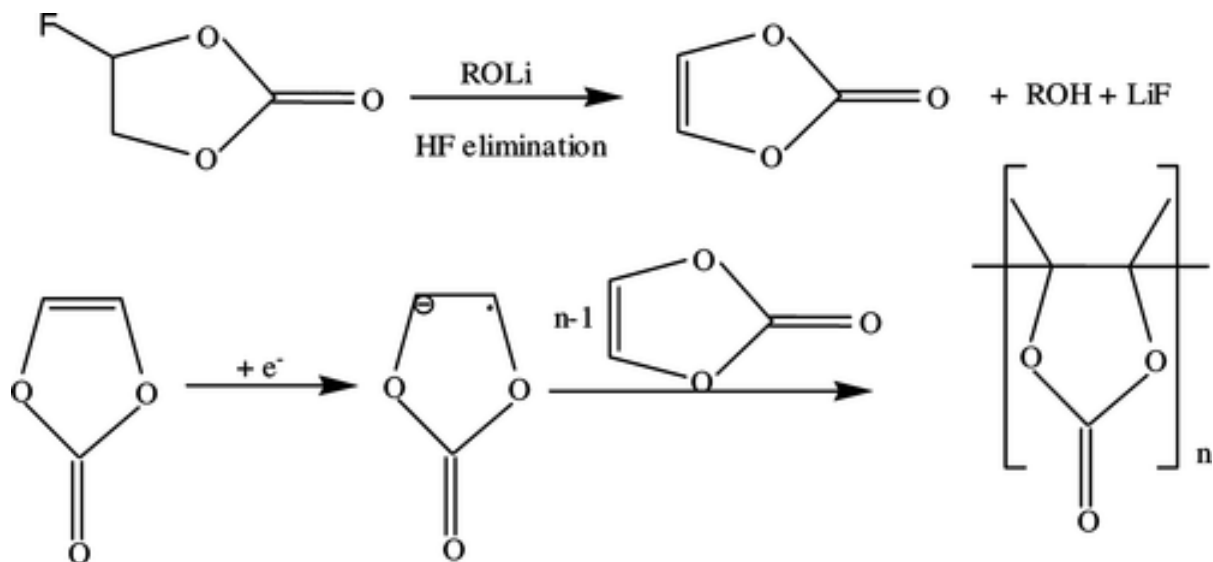


Figure 2.5 Schematic of the decomposition of FEC. ROLi interacts and leads to LiF formation along with  $CO_2$  gas generation. Vinodkumar Etacheri, Ortal Haik, Yossi Goffer, Gregory A. Roberts, Ionel C. Stefan, Rainier Fasching, and Doron Aurbach. Effect of fluoroethylene carbonate (fec) on the performance and surface chemistry of si-nanowire li-ion battery anodes. *Langmuir*, 28(1):965–976, Jan 2012. ISSN 0743-7463. doi: 10.1021/la203712s.

Choosing to promote the formation of LiF formation due to the decomposition of the additive FEC due to LiF films showing improved Mn dissolution [35]. Mn dissolution follows



and destabilises the NMC cathode.

Mn dissolution also promotes cation mixing as mobile Mn ions have poor chemical stability with the electrode and electrolyte material. The formation of Mn side products hinders cell performance by preventing  $Li^+$  migration [35]. An Atomic layer deposition (ALD) of LiF by Tiurin et al. has been shown to prevent Mn passage while promoting Li conductivity. LiF is also a natural choice as a protective coating due to its chemical and electrochemical stability at common cell voltages near 4.2V. The downside to the LiF coating proves to be the decreased Li conductivity of  $1E-23 \text{ S/cm}^2$  [36] compared to that of NMC which is compensated for by keeping the SEI layer ultra thin.

## 2.5 Engineered Growth of the SEI on Electrode Materials

Gao et al. investigated surface modification of the NMC cathode in the attempt to suppress the interfacial parasitic reactions between cathode and electrolyte [37]. NMC622 electrodes were coated with a  $TiO_2$  layer by ALD to act as an chemically stable interfacial layer. The ALD treatment was found to maintain the redox potential of fresh NMC while lowering the cathodic surface film resistance spikes [37]. The parasitic reactions at the CEI were also reduced to the point of mitigated transition metal dissolution and particle fragmentation. Gao et al. also proposed a relationship between interfacial parasitic reactions and the performance loss of NMC cathode devices [37]. Another group has designed in house leakage current measurement system which sheds light on the reaction kinetics between NMC and conventional electrolytes [38]. The rate of parasitic side reactions increases with cut-off potential and a different reaction mode exists above 4.5 V vs  $Li^+/Li$  and that a new method of parasitic reaction suppression must be found to allow NMC to fill fast charging roles.

FEC has also been proven to promote a LiF-rich SEI on Si Li-ion electrodes. Shroder et al. demonstrated that the increased Coulombic efficiency and capacity reduction is due to fluoride ion formation during the reduction of the electrolyte. However, the reaction mechanism is not well understood for all operating conditions. Moreover, the identity of the decomposing species and the reaction pathway to LiF formation is contested [9, 31, 39]. Equation 2.5 depicts the salt decomposition while Figure 2.5 details degradation of the electrolyte solvent. Nonetheless, Juamann et al. also show that the addition of FEC results in the formation of a kinetically stable LiF rich SEI on Si anodes. Surface analysis using XPS and TOF-SIMS showed that FEC forms a thicker LiF-rich SEI, forms  $Li_2O$  and  $LiOH$  species on the Si anode, and decreases the amount of carbon in the SEI [40]. Additionally, FEC increases the Li solubility limit and Li transport properties [7]. This increase in SEI material performance has been attributed to the preferential formation of  $Li_2O$  and LiF. The accumulation of Li at the SEI in the form of these inorganic species also leads to

increased amounts of free Li ions due an enlarged concentration gradient caused by the increased amount of Li at the electrode surface.

In situ NMR spectroscopy (NMR) is another technique that has been used to investigate the effect of the FEC additive on Li deposition for various electrolyte solutions and how the SEI acts to control micro-structural growth [41]. Gunnarsdottir et al. recently used NMR to monitor Li growth during lithium deposition. They showed the FEC additive lead to denser and more uniform Li metal electrodeposits and formed the SEI four times faster with FEC than without [41]. SEI formation is proportional to the exchange current density described by the Butler-Volmer equation. The form of the Butler-Volmer equation

$$j_0 = Fk_0[Li^+]^\alpha[Li^0]^{1-\alpha} \quad (2.10)$$

where  $F$  is the Faraday constant,  $k_0$  is the standard rate constant and  $\alpha$  is the transfer coefficient, describes the exchange current density for Li isotopes. Adjusting the transfer coefficient was demonstrated through the careful choice of material properties of the electrolyte [41]. NMR measurements have shown that Li isotope exchange between the SEI, Li metal, and electrolyte occur simultaneously [41]. This implies that several decomposition pathways are available to  $LiPF_6$  in carbonate based electrolytes.

Tuning the electrolyte interface on Li metal and lithium cobalt oxide (LCO) has been attempted in multiple studies with varying degrees of success [18]. Lee et al. used high concentrations of FEC (30%, 50%, and 70%) with DEC and examined Li/Li symmetric cells using XPS. For increased FEC concentrations the amount of LiF and  $Li_xPO_yF_z$  also increased and the amount of  $LiPF_6$  varies with no discernible trend. Li/LCO half cells with the same concentrations of additive were examined after 10 cycles showing an increase in the C-O-C bond normally attributed to  $Li_2CO_3$ , LiOH, and other carbonate species [29]. The increase in the C-O-C bond also corresponds with the decreased intensity of the M-O peak attributed to LCO [18]. A new peak in the O 1s spectra is also assigned to the polycarbonate decomposition products of VC [18]. Nyquist plots acquired using EIS along with SEM images evidenced the electrode pores being filled with Li metal along with

thicker Li dendrites forming on the Li metal anode. The thicker dendrites also have a smaller surface area which appears to slow the expansion of Li plating [18]. Lee et al. presented Li/LCO batteries with a tuned FEC-containing electrolytes. Cycling stability, capacity retention 97.5%, and Coulombic efficiency 99.0% after 300 cycles were again increased at the cost of an initial drop discharge capacity at concentrations greater than 50% FEC. Discharge capacity dropped due to the formation of a resistive layer on the LCO surface [18].

Zhu et al. found that 10 wt % FEC enables a desirable SEI on MoS<sub>2</sub> and suppresses continuous electrolyte decomposition. Stabilizing the electrolyte with this electrode combination resulted in increased Li reversible capacity of 770 mAhg<sup>-1</sup> for 100 cycles at 1 Ag<sup>-1</sup> attributed to improved Li storage and stable capacity of 510mAhg<sup>-1</sup> at 20Ag<sup>-1</sup> [13]. The initial cycles of the cell with the metal sulfide electrode without FEC showed decreased Coulombic efficiency from the electrolyte degradation. However, the accumulated reaction products form a resistive layer that blocks charge transfer through the SEI and increases the discharge capacity. The Coulombic efficiency of the cell with FEC remained stable with no capacity increase, while the rate capability of MoS<sub>2</sub> also increased [13].

## 2.6 The Merits of the NMC + FEC System and Purpose of Study

As described above many studies have shown the effects of FEC on cycle life and device performance for various electrode compositions and carbonate based electrolytes. However the effects of electrolyte additives on the chemical state of the SEI after the initial discharge cycles has not yet been thoroughly explored for many material combinations. The merits of and outlook on mixed metal oxides reviewed above present NMC622 as an ideal choice of electrode for this study. NMC is commercially available and well understood, but more insight into the initial SEI chemistry is required to fill high power and high energy density demanding applications [6]. Lui et al. showed improved interfacial stability between NMC622 and the electrolyte and demonstrated the formation of a CEI-layer derived from the decomposition of the FEC containing electrolyte and the NMC622 electrode using EIS,

TEM, SEM, and XPS. The effects of 5%, 10%, and 15% FEC additive on discharge capacity and rate performance in the commercially used  $\text{LiPF}_6\text{-EC/EMC/DEC}$  based electrolyte were investigated [27]. After 100 cycles cells were taken apart in an Ar glove box and cycled at a 1C rate at 2.8-4.6 V. NMC/Li cells surprisingly showed increased discharge capacity along with cycle stability. Compared to cells without FEC 60.8%, the cells with FEC had a capacity retention of 87.3%. The increased capacity retention was credited to the oxidation of the 10% FEC additive in the place of the electrolyte solvent [27].

To determine the chemical composition, thickness, and performance of the SEI requires careful analysis of the electrode surface. X-ray photoelectron spectroscopy (XPS) was chosen to determine the chemical and electronic state of the cathode surface species. Electrochemical impedance spectroscopy (EIS) was used to determine the Ohmic and charge transfer resistances of the NMC devices. X-ray diffraction was also used to ensure that no significant crystallographic changes occur during cycling, and scanning electron microscopy (SEM) was used to take a qualitative look at particle cracking. These techniques were chosen to sufficiently investigate the chemical, structural, and electrochemical stability of the CEI.

## CHAPTER 3

### METHODS

#### 3.1 Device Fabrication

Off the shelf Targray NMC cathodes were procured for the FEC concentration study. Cathodes were punched using a 1.5 mm diameter punch, and anodes a 1.3 mm anode punch. The electrodes were then weighed and placed in a vacuum oven at 105C to dry. Stainless steel coin cell parts were also cleaned prior to fabrication. All metal parts were sonicated in IPA for 30 minutes followed by acetone for 30 minutes and another 30 minute round of IPA. The metal parts were then dried in a vacuum oven at 105C while the plastic coin cell gaskets and separators were dried at 70C. All coin cell components including electrodes were dried overnight and quickly moved to an Ar containing glove-box. The cells were assembled as shown in the pictures in Figure 3.1. The cathode cap is lied flat and tweezers are used to place the NMC cathode. After the cathode is placed, 30 $\mu$ l of electrolyte are added. The Celgaard 2500 separator is placed onto the cathode followed by another 30 $\mu$ l of electrolyte. The coin cell gasket is then placed followed by the anode, a SS disk, and SS spring. The anode cab is carefully placed into the stack and the entire assembly is placed in a hydraulic press at 1200 PSI.

##### 3.1.1 Electrolyte Preparation

Electrolyte was prepared using the standard Gen2 formula of 1.2M LiPF<sub>6</sub> in an EC:EMC 7:3 solution and various concentrations of fluoroethylene carbonate by volume. Both the Gen2 electrolyte that was used along with 99.9% FEC were purchased from Sigma Aldrich. 1 mL of Gen2 was placed into dried bottles of known weight to estimate the density of Gen2. With the difference in density of the Gen2 electrolyte and FEC being negligible, appropriate volumes of FEC were added to each bottle by micropipette for 1%, 2%, 5%, 15%, and 30% concentrations.

### 3.1.2 Electrode Fabrication

NMC powder 90%, carbon black Super-P 5% in an N-Methyl-2-Pyrrolidone (NMP) solution, and 5% Polyvinylidene fluoride (PvDF) were mixed together using a high speed Agilent mixer for two 60 second rounds at 1000 rpm. The resulting slurry is then blade coated onto Al foil with a goal of 40  $\mu\text{m}$  thick layer. The Al sheet is then carefully moved into a vacuum oven and dried overnight at 110C. The electrode sheets are punched into shape for coin cells using a an oversized cathode punch as shown in Figure 3.2.

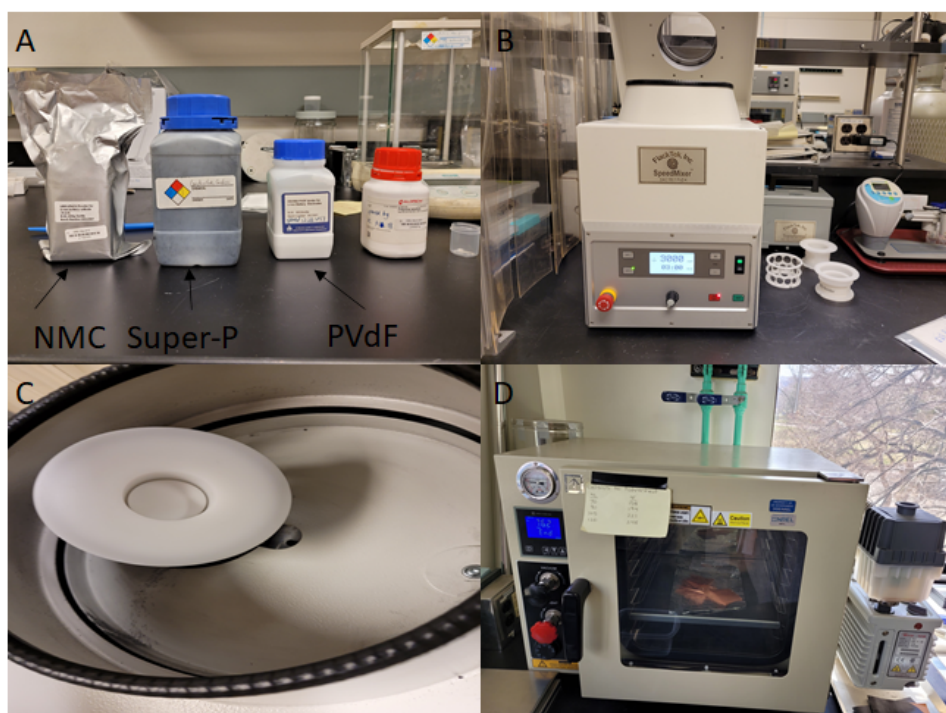


Figure 3.1 From left to right and top to bottom: A Assorted ingredients for electrode preparation including NMC powder in the silver bag, carbon black Seuper-P, and PvDF binder in the white jars, B high speed mixer used to prepare electrode slurry, C inside of high speed mixer, D vacuum oven used to dry electrode at 105C

### 3.2 Cycling and Electrochemical Impedance Spectroscopy

The electrochemical nature of a LiB can be observed by measuring the response of the system to a frequency sweep in alternating current (AC) voltage using EIS. The voltage of the cell at the time of the measurement is chosen to investigate a particular region on the

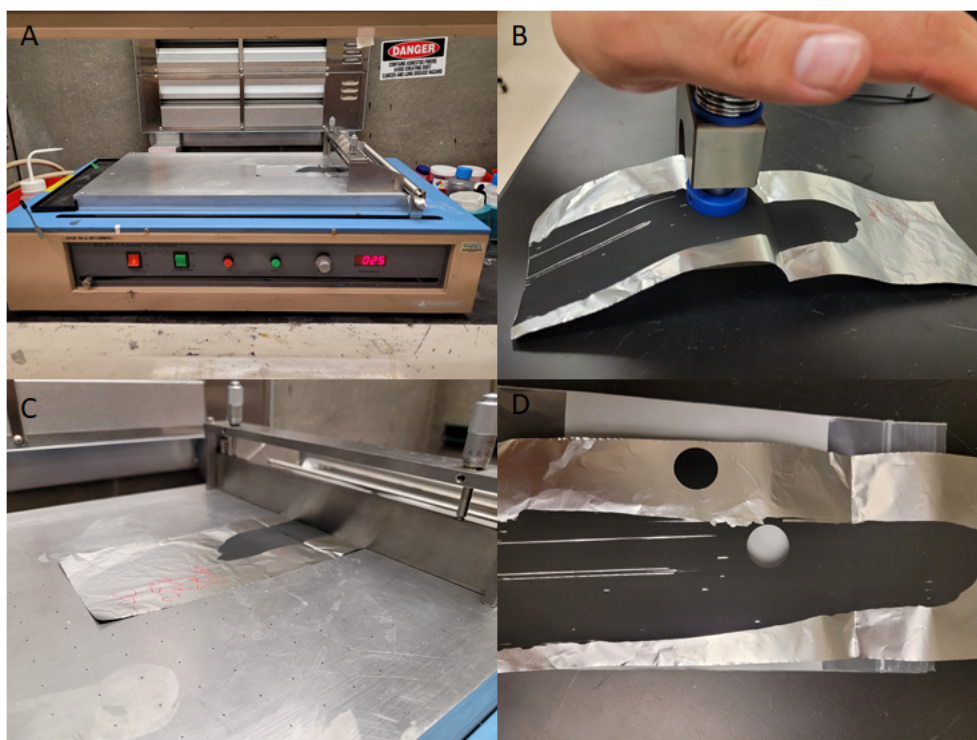


Figure 3.2 From left to right and top to bottom: A blade coating machine used to coat 40 um thick electrodes, B dried electrode sheet punching, C representation of electrode blade coating, D electrode position choice for punch

discharge capacity plot, which for this study was about 4 V. From the resulting data the resistance, impedance, and capacitance of the system can be determined. Impedance  $Z$  can be represented by a complex number

$$Z(w) = \frac{V}{I} = Z_0(\cos \phi + i \sin \phi) \quad (3.1)$$

where  $V$  is voltage,  $I$  is current, and  $\phi$  is the phase shift.

EIS spectra are plotted from high to low frequency with real impedance/resistance as the x-axis and imaginary impedance on the y axis. From the shape and intercepts of EIS semi-circles the combined effects of the electrode electrolyte interface acting as a capacitor and the charge transfer resistance through the interface can be modeled by an equivalent circuit. The circuit in Figure 3.3 is an adapted Randall circuit that has been shown to simulate battery response successfully [42].

For a re-dox reaction



The charge transfer resistance can be determined by using the potential and current.

The equation

$$i = i_0 \left( \frac{C_0}{C_0^*} \exp\left(\frac{\alpha n D \eta}{RT}\right) - \left( \frac{C_R}{C_R^*} \exp\left(\frac{-(1-\alpha)n D \eta}{RT}\right) \right) \right) \quad (3.3)$$

can be used to determine the exchange current density through certain parts of the cell based on the over-potential  $\eta$ , concentration of oxidant species at the surface  $C_0$  and in the bulk  $C_0^*$ , and the concentration of reactant species at the surface  $C_R$  and in the electrolyte  $C_R^*$ . The resistance can be characterized by the exchange current density in 3.3 which simplifies to the Butler-Volmer equation if the concentrations are equal.

For a LiB one of the main modes of transport of the Li ion is diffusion through the electrolyte/electrode interfaces which creates an effect called the Warburg impedance. At low frequencies reactants experience a larger diffusion length which increases the

impedance following

$$\sigma = w^{-1/2}(1 - j) \tanh \left( d \frac{j\omega}{D} \right)^{1/2} \quad (3.4)$$

where  $d$  is the Nernst diffusion layer thickness, and  $D$  is the diffusion coefficient of  $\text{Li}^+$ .  $\sigma$  is the Warburg coefficient which is determined by the concentration and diffusion coefficients of the diffusing species and the surface area of the electrode  $A$ .

$$\sigma = \frac{RT}{n^2 F^2 A \sqrt{2}} \left( \frac{1}{C^{*0} \sqrt{D_0}} + \frac{1}{C^{*R} \sqrt{D_R}} \right) \quad (3.5)$$

The Ohmic resistance is determined by the first intercept of the EIS curve

$$R_{Ohm} = Z_{real} \quad (3.6)$$

and the SEI resistance is determined by the diameter of the first semi-circle. The capacitance of the SEI layer can be determined by the height of the first EIS curve

$$C_{SEI} = \frac{1}{Z_{imag}\omega} \quad (3.7)$$

where  $\omega = 2\pi f$  for an ideal capacitor in an EIS experiment. The constant phase element is a more accurate representation

$$C_{CPE} = \frac{1}{(j\omega)^\alpha Z_{CPE}} \quad (3.8)$$

of the capacitance in a Li-ion cell. The first semi-circle is generally considered to be the anode effects, while the second EIS semi-circle and final linear portion provide insight into the diffusion resistance or Warburg Impedance.

Noise stemming from the EIS instrumentation can change the shape and intercept of otherwise similar samples. The battery connectors and positioning of the reference electrode can affect the noise along with any external electro-magnetic fields generated by other electronics in the lab. Repeating EIS data acquisition is important to determine the distinguishing factors of device impedance and artifacts from the affects described above. Iterating measurement provides a level of confidence in the minor resistance changes between samples.

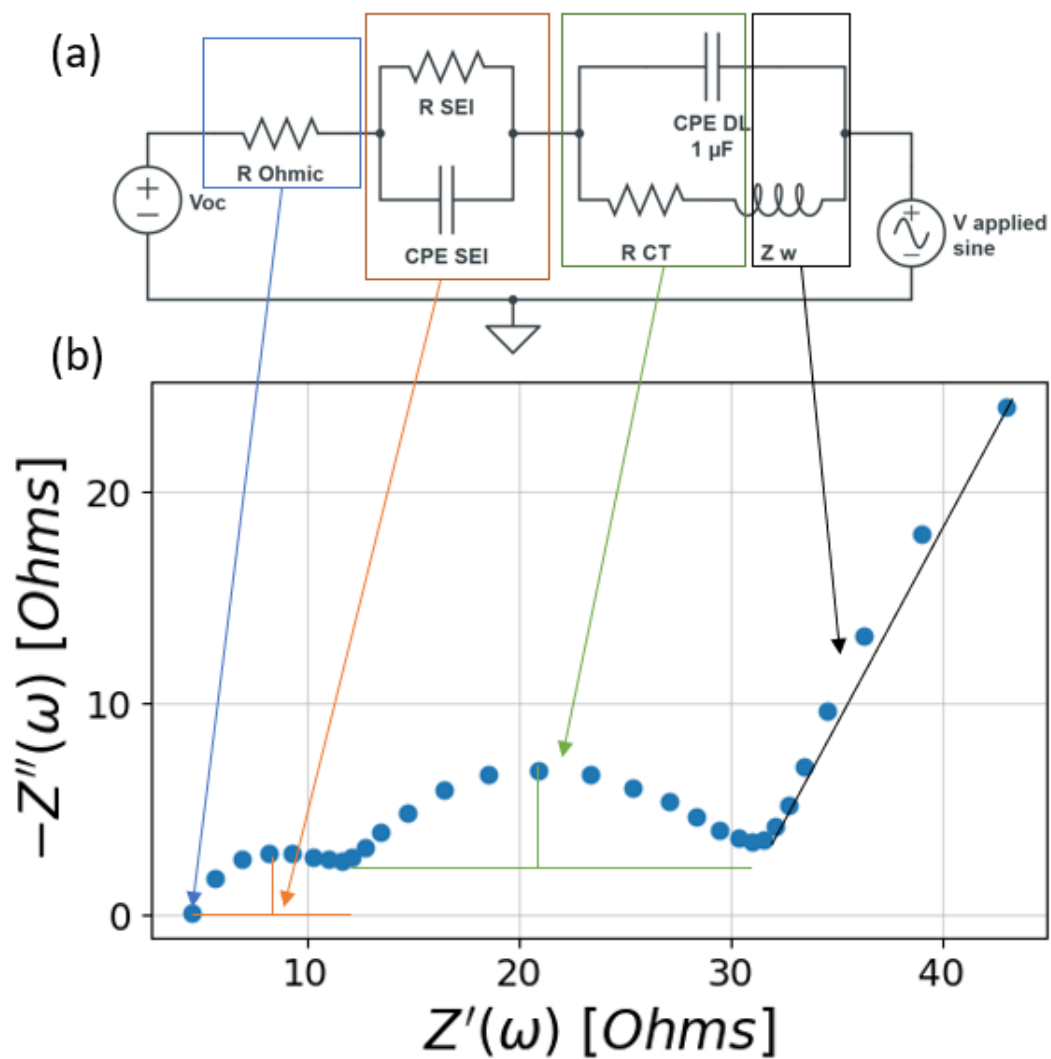


Figure 3.3 (a) shows the equivalent circuit model components and (b) the corresponding EIS response. The cell used in this sample set was cycled using an Arbin cycling cabinet at 4.2V and a C/20 charge rate for 2 cycles. Each cell was then measured near an OCV of 4.2V.

### 3.3 X-ray Photoelectron Spectroscopy

The primary technique used to characterize the surface of the NMC cathode was X-ray Photoelectron Spectroscopy (XPS). XPS is widely used to conduct chemical analysis of solid materials by measuring the energy of primary electrons that are excited by incident photons. The technique is capable of detecting all elements except H and He since these elements do not have primary electrons. XPS can also determine chemical binding states and provides information about the first few nanometers of a material. The small measurement depth is determined by the inelastic mean free path of the photoelectron. The basics for any XPS machine include a ultra high vacuum chamber which contains the electron energy analyser, the x-ray source, and the sample stage. Moreover an electron gun is included in case of charge accumulation and an ion gun is used for cleaning and depth profiling. Often times the ion gun is kept in a separate sample-prep chamber. Qualitative analysis of XPS spectra is supported by tabulated results of energy emission lines in literature. However, quantitative analysis of XPS spectra requires careful peak fitting to support peak area analysis.

#### 3.3.1 XPS Components and Hardware Theory

A more in depth look at the instrumentation required to conduct XPS experiments is necessary to make the connection between the kinetic energy of an electron and the surface chemistry of the sample from which it was liberated. The vacuum system is arguably the most important facet of the XPS machine. If it were to fail many precious components, including the analyser and electronic lenses could be damaged. Furthermore, without ultra-high vacuum conditions the photoelectrons will not travel due to their short inelastic mean free path. The pressure of the system determine the mean free path according to the equation

$$L_{coll} = \frac{kT}{1.414P\sigma_{coll}} \quad (3.9)$$

where  $k$  is the Boltzmann constant,  $T$  is the absolute temperature,  $P$  is the pressure in Pa and  $\sigma_{coil}$  is the cross section of the X-ray collision [43]. Pressure ranging from  $10^{-5}$  to  $10^{-8}$  Torr and  $10^{-6}$  to  $10^{-9}$  Torr are considered high vacuum (HV) and ultra high vacuum (UHV) conditions. HV conditions are sufficient to reduce electron scattering and avoid surface contamination.

Surface contamination caused only by residual gas adsorption can be estimated using the monolayer formation time

$$t_m = \frac{4}{Nvd_m^2} \quad (3.10)$$

where  $N$  is the density of the gas,  $v$  is the monocular velocity, and  $d_m$  is the molecular gas density [43]. In HV conditions surface contamination is unavoidable; however, at pressures lower the  $10^{-6}$  Torr limit the monolayer formation time can be increased. Particularly reactive gases like water vapor, CO, and CO<sub>2</sub> are kept at even lower partial pressures to extend the amount of time required to consider the contamination to be negligible.

In general UHV systems have several pumps. The initial pressure drop is achieved through a mechanical roughing pump. The roughing pump supports ion pumps and/or turbomolecular pumps that reduce the pressure from  $10^{-3}$  Torr to UHV conditions. To move the gas molecules a pressure gradient is set that creates a molecular flow from high to low pressures. The equation for this pump down process is

$$C \frac{dp}{dt} = -Sp \quad (3.11)$$

where  $P$  is the pressure,  $V$  is the volume of the chamber, and  $S$  is the pumping speed [43]. Adding an out-gassing rate  $Q$  to the right hand side of the above equation is more accurate for the pump down process. Out-gassing is primarily caused by the evaporation of samples and deabsorption of adsorbed chemicals from the chamber walls. Out-gassing can be reduced by increasing the temperature of the system during a several hour bake-out to 150-200C. To fulfill the pressure requirements and chemical and oxidative resistances

stainless steel parts are used along with copper gaskets instead of rubber o-rings. Furthermore, carbon contamination must be negated by the use of oil free pumps like the aforementioned ion and turbomolecular pumps. To further mitigate surface contamination an ion gun can be used to clean the surface of any residual gas species. The identity of these species can also be determined by a quadropole mass analyser. The analyser reports the mass of residual gas molecules that the XPS can not detect [43].

Another indispensable part of any XPS machine is the X-ray source. Mg or Al anodes are the most common X-ray sources. The characteristic Mg  $K_\alpha$  radiation at 1253.6 eV and Al  $K_\alpha$  radiation at 1486.6 eV have high enough energy to excite the core level electrons with good resolution. Efficient irradiation requires x-ray sources to be operated from 500W to 1kW and at 5-15 keV excitation voltage. The high powered requirements of the x-ray source also requires that an independent x-ray cooling system be installed. Higher energy resolution can be achieved along with the removal of satellite peaks by using a monochromator. A monochromator selects a single x-ray emission line by the use of quartz mirrors which also focus the x-ray beam [43].

### 3.3.2 Measurement and Analysis

In essence the technique measures the kinetic energy of photoelectrons that are ejected from the surface by high energy x-rays. The x-rays are generated using Al- $k\alpha$  radiation and directed using a single mirror. The incident x-rays are monochromatic meaning they are all the same wavelength and at 1.487 keV in energy. The sample is prepped on carbon tape and placed at  $90^\circ$  to the x-ray source. The liberated photoelectrons travel along differentially pumped chambers through several electronic lenses that focus the beam as shown in Figure 3.4. The analysis chamber is kept below  $1\text{E-}6$  Torr during standard experiments and the slit entrance is kept at  $1\text{E-}9$  Torr. The photoelectrons then travel through a Scienta Omicron semi-hemispherical analyser with a large potential applied across the path. This potential selects the photoelectrons based on the kinetic energy causing them to hit a micro-channel plate followed by a phosphor detector at different path

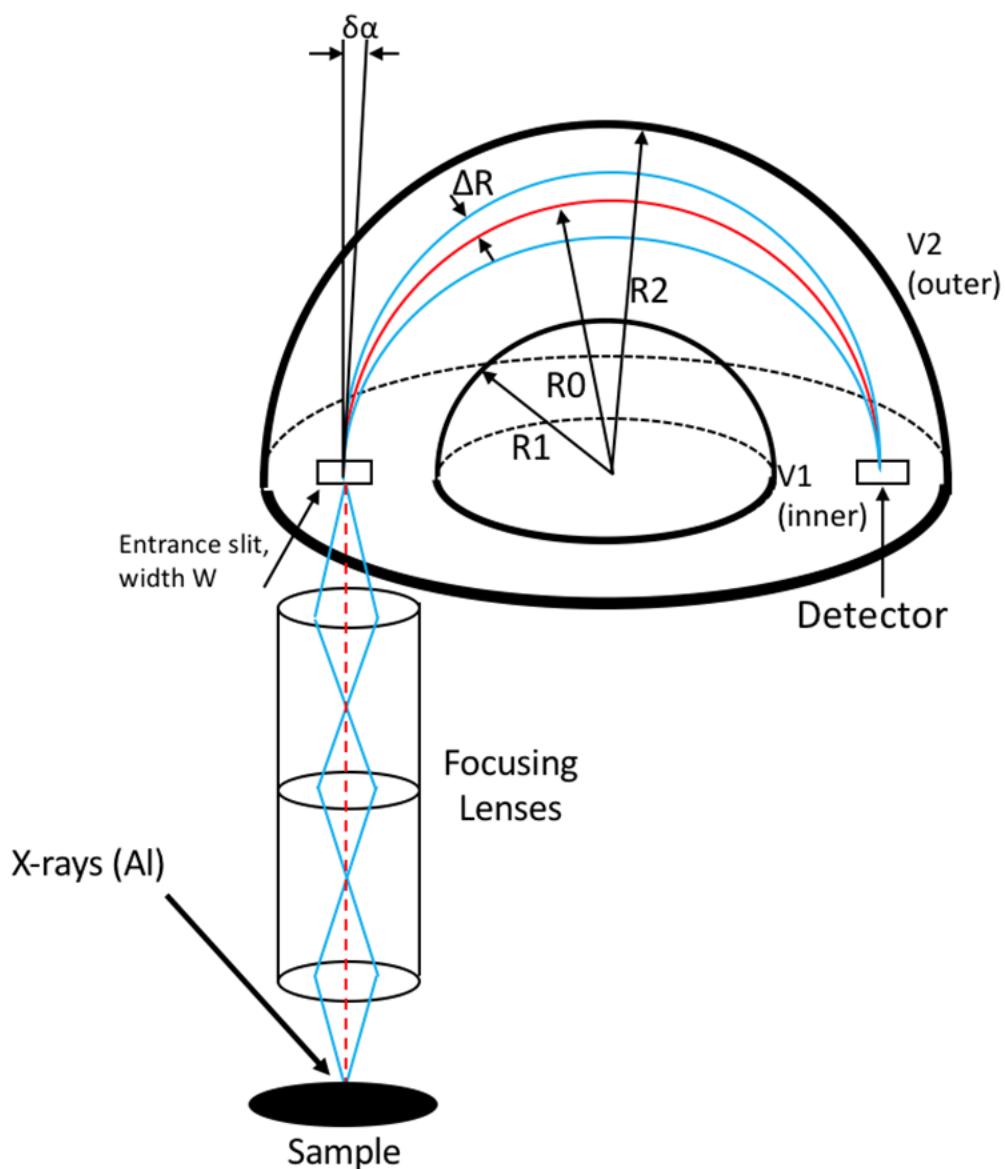


Figure 3.4 Schematic of the XPS showing the incident Al X-rays hitting a black oval sample. The liberated photoelectron path in dashed red follows through the path guided by the Focusing Lenses. The entrance slit of width  $W$  allows the photoelectrons into the semi-hemispherical analyser. A negative voltage is placed at both  $R_1$   $V_1$  and  $R_2$   $V_2$  to select the electrons along  $R_0$  with the  $\Delta R$  which is half the beam width. Reproduced with permission from J. Bass. "Sr Design Poster, X-ray Photoelectron Spectroscopy on Light Emitting Devices", *Department of Physics, Colorado School of Mines, Golden, CO, 2018.*

lengths. The signal is then converted to counts vs binding energy using the well known principle of the photoelectric effect.

$$BE = h\nu - KE + \phi \quad (3.12)$$

with  $h\nu$  being the incident photon energy, and  $\phi$  is any associated phase constant. The phase constant is determined by any charge accumulation or polarization affect on the surface of the sample. Furthermore, the overpotential  $\eta$  of a system can also be estimated using the change in binding energy to calculate polarization resistance changes.

One issue with acquiring XPS data described later in chapter 4 are Auger electrons  $F_{KLL}$  emission lines that are generated and in the spectra near 832 and 858 eV. The  $F_{KLL}$  Auger electrons obscure the Ni 2p signal causing Ni species to be difficult to identify using Al  $k\alpha$  radiation [44]. Switching to a Mg source would alleviate this issue but it is less available. Another issue is surface contamination. Any sample will form a layer of adventitious carbon when exposed to air. NMC samples must be kept in an inert atmosphere to avoid the increased formation of  $\text{Li}_2\text{CO}_3$ ,  $\text{LiOH}$ , and hydrocarbon contaminants.

### 3.3.3 XPS Quantification

To gain meaningful results from XPS data careful quantification must be done in addition to careful peak fitting. In all XPS spectra peaks of interest are supplemented by background counts that must be subtracted out. Common background shapes include the Shirley, Tougaard, and linear backgrounds. The background used in this study is the Shirley background which assumes that the decreasing difference in intensity from higher to lower kinetic energy is based on the inelastically scattered photoelectrons that are detected. The Shirley background adapted from CasaXPS follows the equation

$$S(E) = I + k \frac{A2(E)}{(A1(E) + A2(E))} \quad (3.13)$$

where the determination of  $S(E)$  is an iterative procedure.  $A1(E)$  and  $A2(E)$  are determined using integration of the data set for different intensity steps  $k = \Delta I$ , where  $I$  is the intensity of the spectral peaks. Often times XPS spectra will have peaks that overlap to a lesser extent than described above with  $F_{KLL}$ . The overlapping peaks arise due to the presence of different elements or different chemical states [43]. Careful fitting of standard Gaussian or Gaussian-Lorentzian mixture line shaped were used in this study once the background was determined. The peak data was analysed and prepared using python scripts which leverage NumPy, pandas, lmfit, and matplotlib to generate the original figures found in this document. Peak centroids, FWHM, gamma, amplitude, and relative ratios were all carefully controlled using the fitting algorithm, written by the Author and shown in appendix A, to decompose any overlapping peaks.

To determine the atomic composition of a sample from XPS spectra requires using elemental relative sensitivity factors (RSF). For a sample consisting of multiple elements the atomic concentration ratio of elements A and B is

$$\frac{X_A}{X_B} = \frac{I_A/I_A^0}{I_B/I_B^0} = \frac{I_A}{I_B} S_{B,A} \quad (3.14)$$

where  $I$  is the measured intensity, and  $S_{B,A}$  is the RSF of element A relative to element B [43]. For constant instrument parameters samples composed of a pure element can be used to determine the mole fraction of that element in a compound based on the relative intensity between the element peaks. These RSF values are tabulated for specific empirical conditions and can be used to calculate the atomic composition. For example, the RSF value for the F 1s peak is 1.000 at 90C, so the intensity of F 1s in a pure fluorine sample will be the same as the intensity of F 1s in a LiF sample. If every element in a sample is characterized by at least one XPS peak, then the atomic composition of the sample surface is determined for each element X following

$$X_1 = T(E) \frac{I_1}{\sum S_1/S_i I_i} \quad (3.15)$$

where  $I$  is the peak intensity,  $T(E)$  is the transmission function, and  $S$  is the corresponding RSF [43].

Another important facet of peak analysis is the chemical or electronic shift of photoelectron peak energy. For conductive materials charging effects can largely be ignored in XPS, while insulating materials require charge neutralization to counteract changes in peak position. Chemical shifts as seen by the change in binding energy position and peak widths can be caused by any change in the bonding state of the sample. The shift is able to be estimated by the change in electronegativity between two bonding states of an element. A more accurate depiction of the chemical shift observed in XPS spectra includes screening effects. A photoelectron can be screened by scattering due to collisions with the atomic electrons left behind. The scattering effect can be influenced by phonon interactions, charge interactions, and electron cloud shape/size [43].

### 3.4 X-ray Diffraction

X-ray Diffraction (XRD) is an experimental technique used to determine the atomic and molecular structure of a crystalline substance. The method measures the intensity of x-rays that have diffracted off the surface of a material over a range of angles. The resulting spectra details the electron density at certain crystal planes. The diffraction pattern discerned from the peak location, intensity, and shape can be used to determine the crystal structure, chemical bonds, and crystallographic order. XRD can also provide insight into the electronic and mechanical properties of materials.

To ensure any performance changes in the NMC cathode were not caused by bulk structural changes of the cathode XRD was performed. Monochromatic X-rays are generated and narrowed using an anti-scatter slit and the diffraction slit. A standard  $2\theta$  gonio scan is used to determine the crystallographic structure of the NMC samples. The incident beams diffract according to the Bragg relation

$$n\lambda = 2d \sin \theta \tag{3.16}$$

where  $\lambda$  is the incident wavelength, and  $d$  is the distance between crystal planes. The wavelength of the diffracted length is measured over a range angles which result in a spectra with peaks for every crystallographic plane. These peaks can then be used to determine the structure of the material [45]. The applications of XRD to NMC cathodes also include insights into cation mixing and Li migration using peak width changes and peak intensity ratios.

### **3.5 Scanning Electron Microscope**

Scanning electron microscopy (SEM) was also used to verify the structure of the electrode surface. A SEM creates high resolution and high magnification images using an focused electron beam. The electrons interact with the atoms of the material surface and cause other backsattered or secondary electrons to return to a detector near the beam source. The position and intensity of the incident and detected electrons give information about the surface topography including roughness, particle shape, and surface composition. The penetration depth of the electrons along with an the wide view of the SEM can also be used to further understand the macroscopic structure.

CHAPTER 4  
INVESTIGATING THE CONTRIBUTION OF FLUOROETHYLENE CARBONATE TO  
CELL STABILITY IN  $\text{LiNi}_{0.6}\text{Mn}_{0.6}\text{Co}_{0.2}\text{O}$  CATHODE CONTAIN LI-ION  
BATTERIES

Note: This chapter is in preparation for publication

#### 4.1 Focused Introduction

For energy production to move away from fossil fuels and towards renewable sources, a reliable energy storage solution is needed. As shown in chapter 2 a promising technology to fill this role is the ever-advancing Li-ion battery. LiBs are a reliable solution that would supplement intermittent power generation from renewable sources by providing voltage stability during peak demand hours [46]. LiBs are highly sought after in the energy sector for grid applications due to the low energy loss (5% per month) of these systems [2]. To improve upon conventional cell design the mechanisms of degradation of the active material and electrolyte in Li-ion batteries must be better understood. In recent years the performance and stability of Ni-rich cathodes like  $\text{LiNiMnCoO}$  (NMC) have been extensively studied. NMC shows promising performance for fast charging applications due to a theoretical capacity of 275 mAh/g, an ionic conductivity on the order of  $1 \text{ mScm}^{-1}$ , and an electrochemical stability of 4.3 V vs Li/Li<sup>+</sup> [4]. NMC-622 has a practical specific discharge capacity of 160 mAh/g and can provide both the high energy and power densities needed for ancillary grid applications [46]. When NMC is paired with the electrolyte  $\text{LiPF}_6$  in EC a heterogeneous SEI composed of primarily  $\text{LiF}$ ,  $\text{Li}_2\text{CO}_3$ , and  $\text{LiOH}$  forms on the cathode surface via electrolyte degradation. The degradation of the  $\text{LiPF}_6$  salt is determined by the amount of  $\text{LiPF}_6$  in the electrolyte, charge rate, cell voltage, and parasitic reactions with any trace water contaminant. With all other parameters constant (mass, structure, active material), increasing the cell voltage and charge rate will increase

the degradation rate of LiPF<sub>6</sub>, which can be measured by observing the formation of LiF at the NMC cathode surface. To improve the performance of these systems, novel electrolyte systems and electrode coatings are still being developed to improve the capacity and stability of Li-ion batteries.

To charge quickly the cell will need to withstand high current rates and voltages above the reported electrochemical stability of 4.3V. Currently when the 4.4V threshold is surpassed, the cathode particles begin to crack and undergo pulverization [10]. Furthermore LiF formation [24], transition-metal dissolution [9], anisotropic volume change [5], chemical crossover [20], electrolyte oxidation [7], and Li plating [41] all contribute to capacity fade at different states of charge. Li et al. report that transition metal dissolution and chemical crossover have greater prominence at 4.4-4.5V, whereas at 4.2V these mechanisms do not contribute to capacity fade. Instead, performance loss at lower voltages is attributed to particle cracking and the chemical degradation of the electrolyte. Li et al. also propose several mitigation strategies including cathode/anode doping, electrolyte additives, grain boundary strengthening, novel electrolyte systems, and a better understanding of material level performance. The formation of LiF via the decomposition of LiPF<sub>6</sub> lowers cell capacity by removing the amount of active material [47]; however, as seen in Figure 2.3 Park et al. have shown that a LiF rich SEI on the anode of NMC/Li cells promotes electrolyte stability resulting in longer cycle life [11]. The degradation mechanism of LiPF<sub>6</sub> in Li/Li symmetric cells has been shown to create a dead Li layer on the metal anodes followed by a LiF containing SEI [8], but the mechanism for LiF growth on NMC has not been extensively studied. For example Park et al. showed that the fluorinated solvent EMC:FEC(3:1) reduces the thickness of the dead material compared to EC:EMC(3:7) solvents. The electrolyte additive FEC combined with an EC based electrolyte promoted cell stability by encouraging the growth of a LiF rich CEI [30]. The formation of LiF, by the widely accepted decomposition reaction of LiPF<sub>6</sub>, lowers cell capacity by removing the amount of active material. However, Park et al. have shown that

a LiF rich SEI on the anode of NMC/Li cells promotes electrolyte stability resulting in longer cycle life. To investigate LiF formation and its effects on the phase evolution and morphology of NMC a suite of surface science techniques were used including X-ray Photo-electron Spectroscopy (XPS) and X-ray Diffraction (XRD), and Scanning Electron Microscopy (SEM). The performance and electrochemical characteristics of the cells were measured using and Electrical Impedance Spectroscopy (EIS).

The Li ion device performance can be correlated to the formation of an increasingly LiF rich layer by measuring the relative concentration at the surface using XPS. The effects of a tuned LiF-rich CEI in NMC/Graphite coin cells have not been extensively studied. Improving cell stability by promoting the growth of LiF on the NMC cathode by adding small amounts of FEC as an electrolyte additive provides new insight into the initial chemistry and electrochemistry of the CEI. Moreover, estimating the polarization of the LiF-rich CEI by carefully quantifying XPS peak shifts and correlating the phase constant to the B-V equation provides a novel mode of electrochemical analysis.

## 4.2 Results

### 4.2.1 Device Cycling and Electrochemical Impedance Spectroscopy

To test if NMC/graphite cells are more stable when FEC is used as an electrolyte additive EIS was performed on cells that have been cycled at 4.2V with and without FEC. The trends observed in capacity retention, impedance growth, and cell life have been used to validate increased cell stability. These values were then used in equations 4.1 and 4.2 to estimate the thickness of the LiF layer and the  $\text{Li}^+$  ion conductivity through the LiF CEI. Equation 4.3 is a standard version of the Butler-Volmer (BV) equation used to estimate the expected overpotential across the CEI and NMC cathode.

$$d_{LiF} = C_{LiF} \frac{n_{LiF}}{N_{Li} \rho_{LiF}} \tag{4.1}$$

where  $d_{LiF}$  is the thickness of the LiF layer,  $C_{LiF}$  is the LiF layer capacitance,  $n_{LiF}$  are moles of LiF,  $N_{Li}$  is the concentration of free Li ions, and  $\rho_{LiF}$  is the density of the LiF

SEI. The thickness of the SEI can then be used to determine the Li conductivity coefficient through the LiF rich SEI layer.

$$K_{SEI-LiF} = \frac{d_{SEI} J_{app}}{\eta} \quad (4.2)$$

where the overpotential  $\eta$  is given by the BV equation

$$i = i_0 \left( \exp\left(\alpha \frac{nF}{RT} \eta\right) - \exp\left(-\left(1 - \alpha\right) \frac{nF}{RT} \eta\right) \right) \quad (4.3)$$

As shown in Figure 4.1 the cycling capabilities of the FEC containing cells were similar for the first cycle (A). Upon finishing the second formation cycle the discharge capacity of 2% 15%, and 30% FEC increases from 97.09 mAh/g to 116.09 mAh/g, 120.63 mAh/g to 125.86 mAh/g, and 109.20 mAh/g to 117.25 mAh/g. The 1%, 5% decreases from 133.39 mAh/g to 126.32 mAh/g and 133.814 mAh/g to 74.77 mAh/g. Moreover the 5% FEC cell has both the best and worst performance from the two different set of cells. 5% FEC shows an increase in discharge capacity at the end of the second cycle for the first set of cells, but also experiences rapid capacity fade and voltage fade in the second set. The decrease in discharge capacity for the first set of cells corresponds with the increase in cathode resistance shown in Figure 4.1. The voltage drops at the beginning of the discharge cycle increase with FEC concentration, which can also help explain the deviation in discharge capacity and the correlation between FEC concentration and discharge capacity.

Table 4.1 Resistance values for the Ohmic, SEI, and charge transfer components of the EIS curves. The capacitance of the SEI is also reported. All values are shown for 1%, 2%, 5%, 15%, and 30% FEC after the initial discharge cycles.

FEC Loading	R Ohmic $\Omega$	RSEI $\Omega$	R ct $\Omega$	C SEI $\mu\text{F}$
1%	4.9	6.5	14.9	6.5
2%	4.6	6.5	19.3	6.5
5%	4.5	12.2	12.2	12.2
15%	5.5	7.2	17.9	7.2
30%	7.4	16.2	10.9	16.2

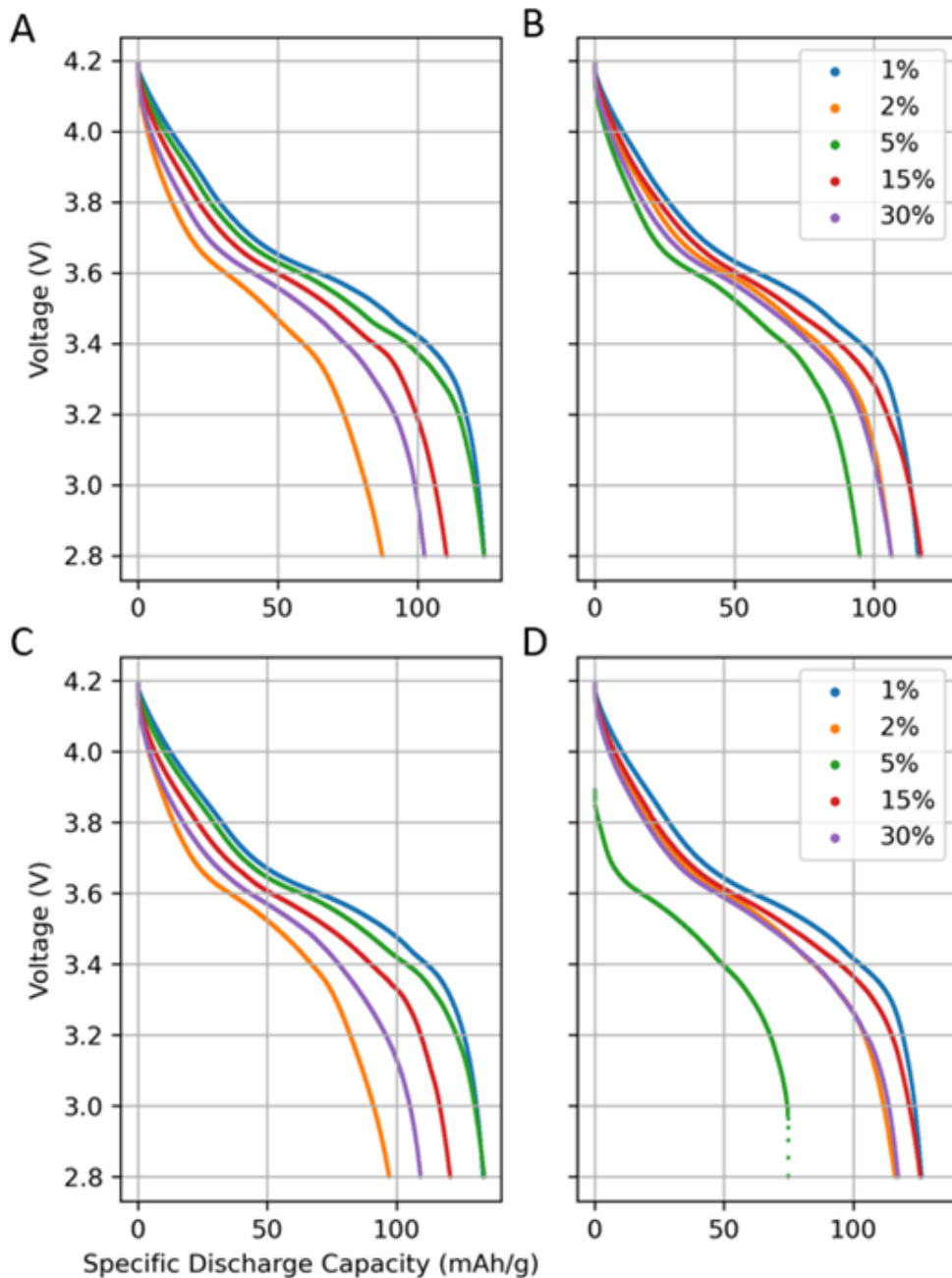


Figure 4.1 (a) is the first formation cycle for 1%, 2%, 5%, 15%, and 30% FEC concentrations in blue, orange, green, red, and purple respectively showing a large discharge capacity distribution. (b) is the first formation cycles for the second set of cells which show a tighter capacity distribution. (c) is the second formation cycle for the first set of cells which show the same wide capacity range but also show increased capacity for all FEC concentrations. (d) is the second formation cycle for the second set of cells which shows the tightest capacity distribution and the highest overall capacity except for 5% concentration which failed (possibly due to excess water contamination)

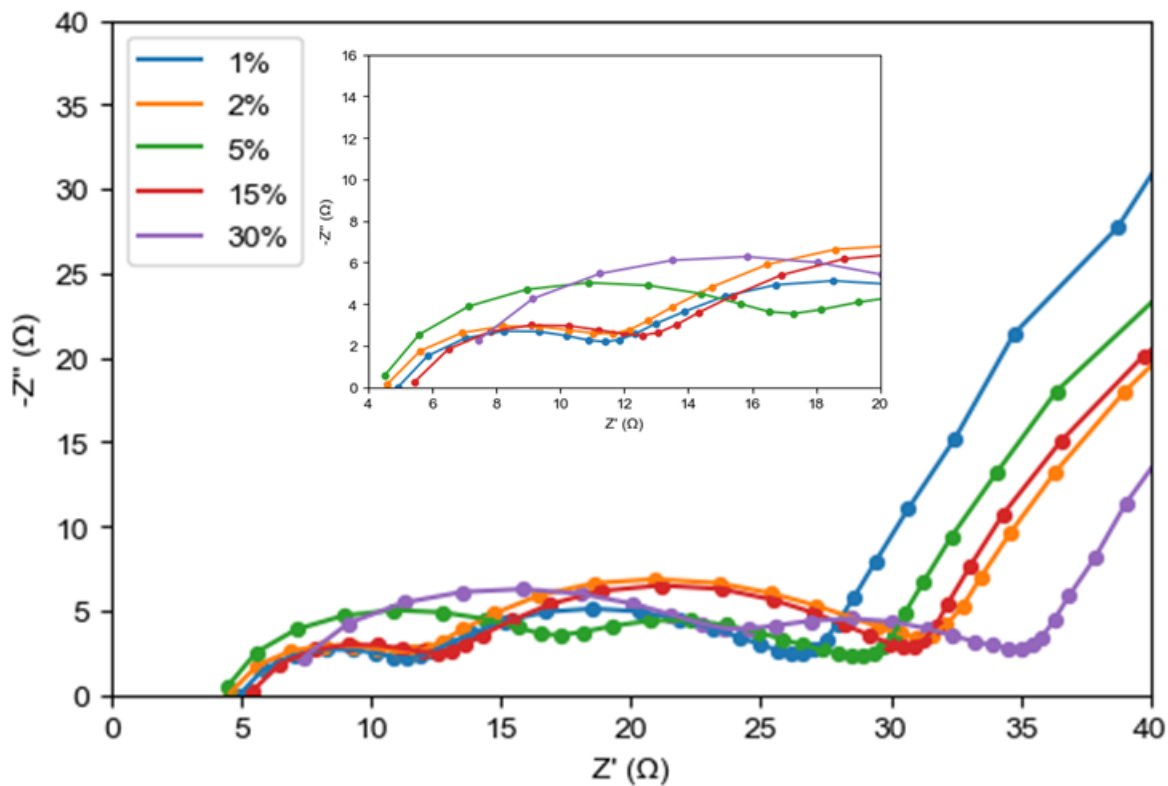


Figure 4.2 EIS curves for 1%, 2%, 5%, 15%, and 30% FEC containing cells in blue, orange, green, red, and purple. Data has been presented as to highlight the initial wide semi-circles associated with the cathode SEI. The purple curve 30% FEC begins at  $7 \Omega$  while the rest of the curves begin near  $5 \Omega$  which can be attributed to noise in the measurement system. The characteristic semi-circles have uniquely elongated shapes and large Warburg impedance.

The anode SEI resistance as measured by EIS for 1%, 15%, and 30% all fall between 12-14 Ohms while the anode resistance for 2% and 30% are 17 Ohms and 25 Ohms respectively. The charge transfer resistance at the anode for 1%, 15%, and 30% are also close in value compared to the other samples. Assuming that the thickness of the LiF layer in the CEI is the main factor affecting the anode SEI resistance, then the LiF accumulation for 1%, 2%, and 15% are similar while the 5% and 30% concentration have a larger first arc contributed to the anode impedance.

The impedance of the cathode side of the battery can be inferred from the second semi-circle. The 2% and 15% FEC loadings show the largest and have quite similar diameters for the second-semi circle. 1%, 2% and 30% seem to vary with no apparent connection to FEC loading. Moreover, the 30% curve shows the largest initial semi-circle and the smallest secondary semi-circle. The linear portion for each FEC loading shows comparable diffusion resistance or Warburg impedance. Table 4.1 details the results equivalent circuit modeling. The Ohmic resistance nominally increases with FEC concentration with 1%-5% having about 5  $\Omega$  of resistance, and 30% 7.4  $\Omega$ . The resistance of the SEI is the 6.5  $\Omega$  for 1% and 2% FEC loading. 4% and 30% FEC loading show the largest SEI resistance with 12.2  $\Omega$  and 16.2  $\Omega$  respectively. The 15% FEC loading has a small SEI resistance compared to its charge transfer resistance of 17.9  $\Omega$  which is only second to the charge transfer rate of the 2% FEC loading of 19.3  $\Omega$ . 5% and 30% also share an increased double layer capacitance at the SEI with 12.2  $\mu\text{F}$  and 16.2  $\mu\text{F}$ . Moreover, the 30% FEC loading has the smallest charge transfer resistance while taking the largest increase in Ohmic and SEI resistances along with the SEI capacitance.

#### **4.2.2 Scanning Electron Microscopy and X-ray Diffraction**

XRD spectra as shown in Figure 4.4 were acquired to verify that the crystal structure of the NMC cathode was not affected by the FEC additive. The 003/104 peak ratios for the 1%, 2%, and 15% concentrations were above 1.3 while the peak ratio for 5% and 30% fell slightly below 1.3 indicative of minor cation mixing. The background for the 5% and

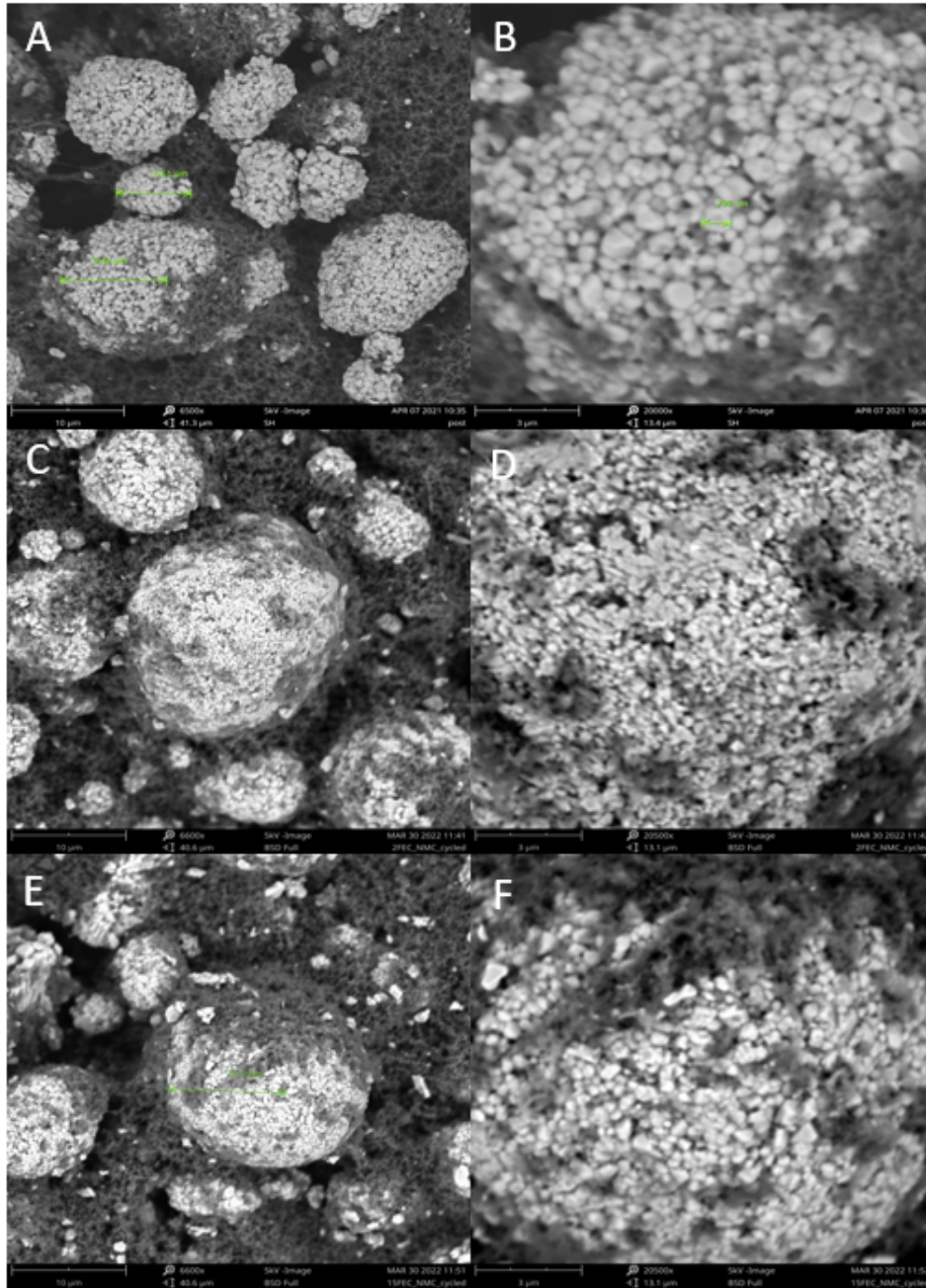


Figure 4.3 SEM images of fresh NMC electrode depicting particles of various sizes. (A) NMC particle distribution in the binder material, 10 μm scale at 6500x magnification gathered at 5keV. (B) 3 μm scale at 20000x magnification at 5kV electron excitation voltage. (C) SEM image of cycled electrode in 2% FEC showing minor particle pulverization 10 μm scale at 7000x magnification. (D) cycled electrode in 2% FEC 3 μm scale at 20500x magnification at 5kV electron excitation voltage. (E) SEM image of cycled electrode in 15% FEC showing minor particle pulverization 10 μm scale at 7000x magnification. (F) cycled electrode in 15% FEC 3 μm scale at 20500x magnification at 5kV electron excitation voltage. Light gray portions are NMC particles while darker gray and black portions are binder material and carbon black.

30% seen in the XRD spectra had increased intensity compared to the other concentrations. Furthermore, the 006/012 and 018/110 doublets have unique shapes above 5% FEC concentration which can be caused by phase transformations. Figure 4.3 shows

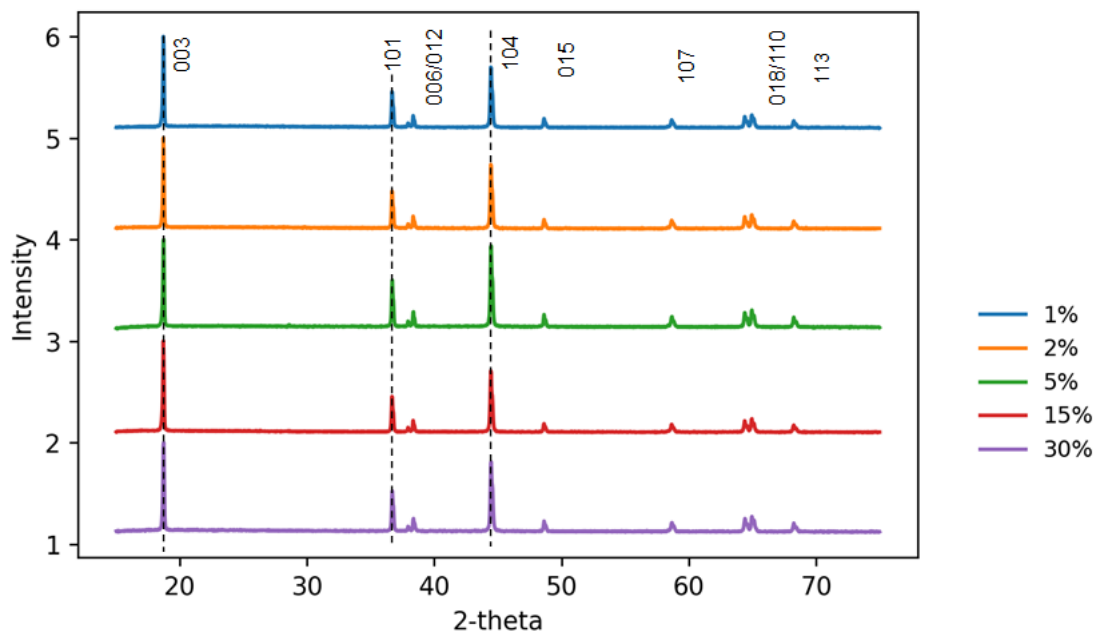


Figure 4.4 XRD spectra normalized to the (003) peak to be 1. Spectra plotted for each FEC concentration 1%, 2%, 5%, 15%, and 30% in blue, orange, green, red, and purple. Miller indices for identified peaks are shown above the corresponding diffraction peak. Dashed black lines indicated no significant peak position changes. Peak assignment fits with the well known layered  $\text{Li}_x\text{MO}_2$  type of NMC structure, with a space group of R-3m.

SEM of fresh and cycled NMC cathodes. The images show light gray NMC particles surrounded by black binder material. The diameter of the NMC particles range from 6 $\mu\text{m}$ -20 $\mu\text{m}$  and are formed from smaller sub particles on the order of several hundred nanometers to 1 $\mu\text{m}$ . The binder material is non-uniformly distributed over the surface of the particles making a rough surface with depression in the binder material appearing black. The second SEM image further shows the structure of the super-particle and small patches of binder material. The shape of the smaller particles appears to be primarily

rectangular shape with the larger particles taking the characteristic NMC sphere.

### 4.2.3 X-ray Photoelectron Spectroscopy

To investigate the accumulation of LiF on the CEI of these cathodes XPS measurements were taken on both electrodes that have only been exposed to the varying FEC electrolyte concentrations and electrodes that have been cycled with varying FEC electrolyte concentrations. The chemical composition of the SEI was investigated using XPS. The surveys in Figure 4.5 and Figure 4.6 show the same elements for all concentrations of FEC. A qualitative look shows that the 2% FEC has decreased intensity for every peak while 5% FEC has the highest relative concentration of carbon. The atomic concentrations are summarized in Table 4.2.

Table 4.2 Relative atomic concentrations calculated from F 1s, C 1s, O 1s, and P 2p for 1%, 2%, 5%, 15% and 30% FEC loading for both washed and cycled electrodes along with Gen2 control for the washed electrodes

Washed Electrodes							
Element/CL	RSF	Gen 2	1%	2%	5%	15%	30%
Fluorine 1s	1	80	83	80	84	78	83
Carbon 1s	.296	13	13	13	13	14	7.0
Oxygen 1s	.711	7.0	4.0	7.0	3.0	8.0	1.0
Phosphorous 2p	0.412	0.00	0.00	0.00	0.00	0.00	0.00
Cycled Electrodes							
Fluorine 1s	N/A	N/A	85	84	81	87	71
Carbon 1s	N/A	N/A	7.0	10	12	9.0	21
Oxygen 1s	N/A	N/A	7.0	15	9.0	9.0	9.0
Phosphorous 2p	N/A	N/A	0.00	0.00	0.00	0.00	0.00

The cycled electrodes in Figure 4.6 show a large spike in intensity for the fluorine and carbon content compared to the washed electrodes. In both sample sets the transition metals show decreased prominence due to the accumulation of fluorine and carbon.

A closer look at the F 1s core level in Figure 4.7 show large BE peak shifts to lower energy for the 2% FEC loadings in panels B and G. Concentrations of FEC over 5% show peak shifts beginning to propagate in the other direction towards higher binding energy.

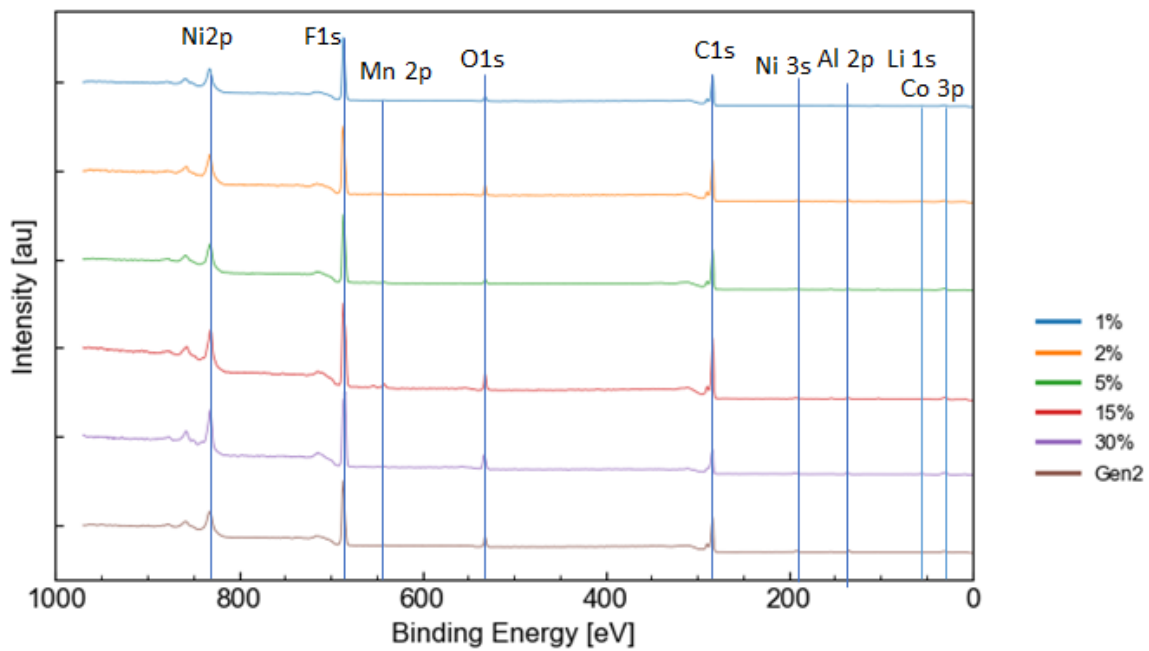


Figure 4.5 XPS survey for Washed electrodes of varying FEC concentrations 0%, 1%, 2%, 5%, 15%, and 30% in blue, orange, green, red, purple, and brown. Surveys are plotted together to highlight peak centroid changes and overall intensity differences. Peaks are labeled with assigned core levels Ni/F, F, O, C, Mn, Al, Li, and Co.

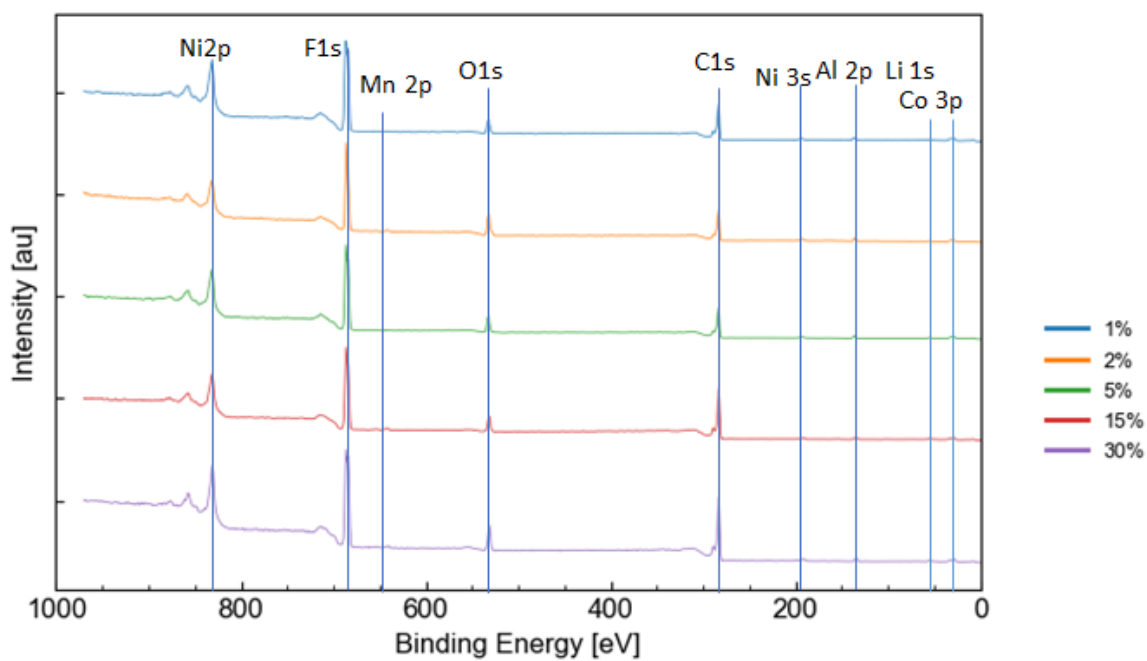


Figure 4.6 XPS survey for cycled electrodes of varying FEC concentrations 1%, 2%, 5%, 15%, and 30% in blue, orange, green, red, and purple. Surveys are plotted together to highlight peak centroid changes and overall intensity differences. Peaks are labeled with assigned core levels Ni/F, F, O, C, Mn, Al, Li, and Co.

The relative intensity of the LiF peak increases with FEC loading for the washed electrodes but varies in intensity for the cycled electrodes. The peak model locked the FWHM of both peaks for all F 1s spectra. The green peak assigned to the binder material near 687 eV has the same relative intensity for all FEC concentrations implying that the binder material has level of chemical stability during initial cycling. The C 1s core level plots reveal complex carbon chemistry at the surface of the cathode. Both the binder material, electrolyte decomposition products, and solvent decomposition products appear as C-C, C-C=O, and C-O bonds. between 283-287 eV. The brown C-F peak at 290.1 eV shows consistent shape and width, but the entire C 1s spectrum does shift. The intensity of the purple peak associated with some hydrocarbon bond also appears to increase with FEC loading.

The accumulation of LiF for the electrode only sample set is linear with FEC concentration except for the 2% FEC concentration in panel A for the (PFx+PvdF)/LiF ratio. The cycled electrode sample set is also linear apart from the 1% FEC. Following equation x with all other variables held constant the concentration of LiF depends on the RC time constant of the as determined by EIS and the electric flux through the LiF layer. The LiF/Total Area ratio in panel B shows that LiF growth is indeed encouraged by the addition of FEC. However, when compared with panel A the overall growth rate of LiF must also be affected by the decomposition of the LiPF<sub>6</sub> electrolyte. Moreover, a drastic difference appears for the LiF concentration in the 1% between cycled and non-cycled electrodes. The cycled electrodes have an increased amount of LiF formation whereas 2%, 5%, 15%, and 30% are within the error spread for both test cases. At 5%-15% the cycled electrode experiences a near horizontal trend in LiF concentration while the electrode only sample experiences a shallow rise. The crossing point between 5-15% occurs in the C 1s and P 2p plots below but at different points. This implies that there is a multi-step chemistry occurring around 5% FEC concentration. The crossing point can also be attributed to the clear growth of PFx in panel A. Figure 4.8 shows that the amount of C-F in the CEI or at least in the electrode is relatively constant with FEC concentration as the

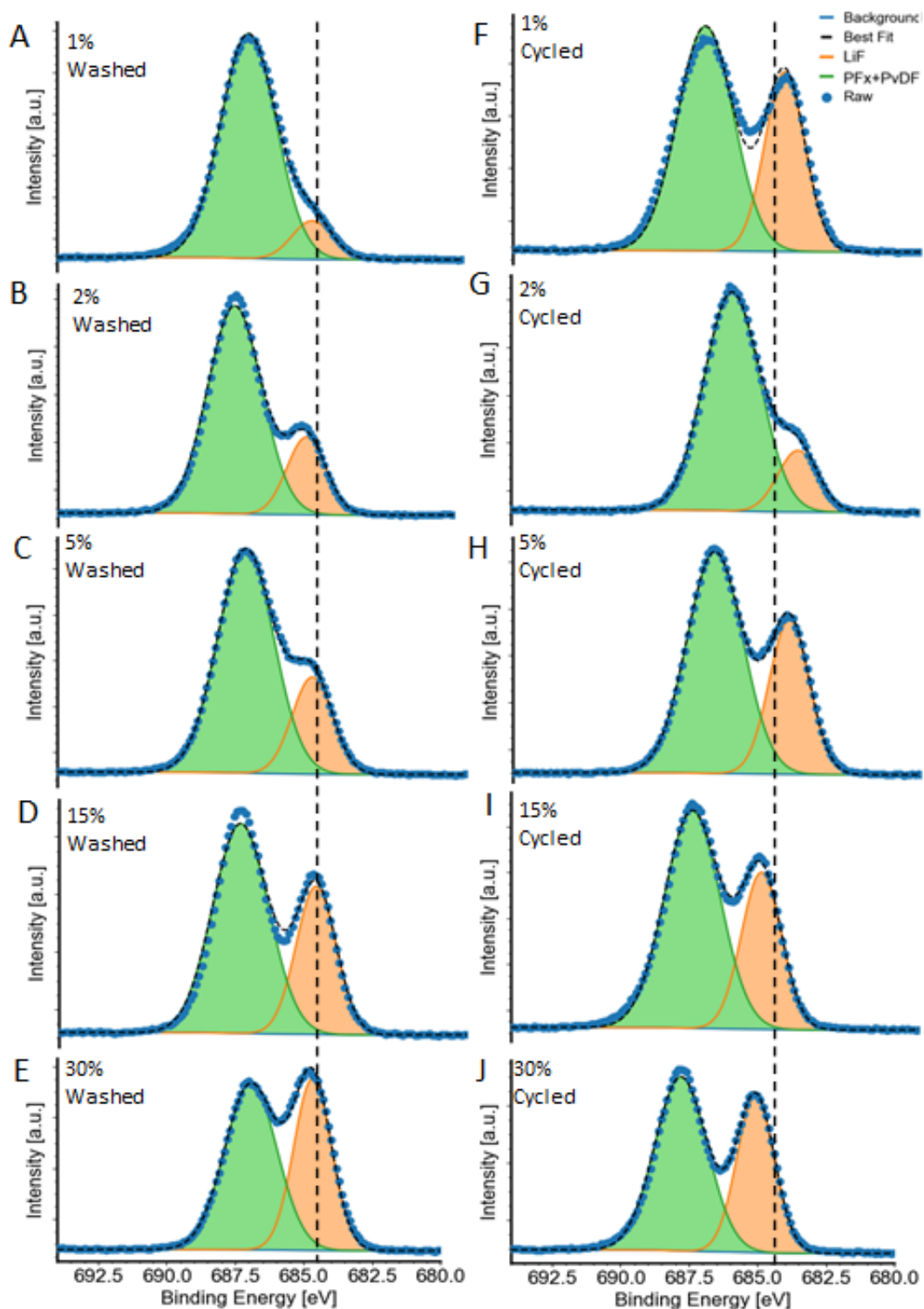


Figure 4.7 XPS spectra of F 1s core level gathered from 694-680 eV plotted on individual y-scales. (a) is a washed electrode with 1% FEC concentration with LiF peak in orange and binder + electrolyte decomposition peak in green as is the same for all panels. (b) 2% FEC concentration, (c) 5% (d) 15%, (e) 30%. The right column contains (f) a cycled electrode for 1%FEC concentration followed by (g) 2%, (h) 5%, (i) 15%, and (j) 30%

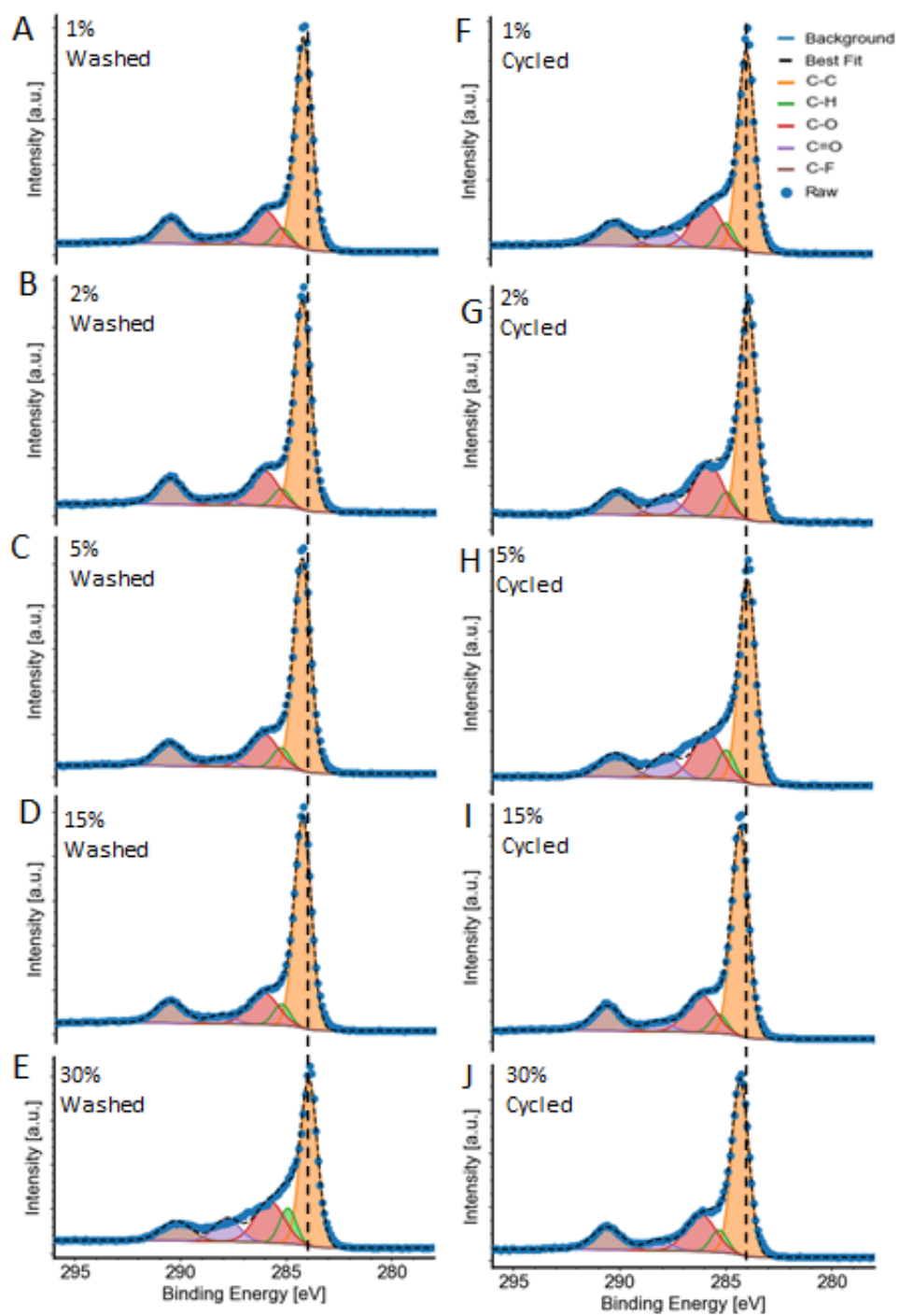


Figure 4.8 XPS spectra of C 1s core level gathered from 296-278 eV plotted on individual y-scales. (a) is a washed electrode with 1% FEC concentration with C-C peak in orange, H-C-O bond in green, C-O bond in orange, and C-F bond in brown as is the same for all panels. (b) 2% FEC concentration, (c) 5% (d) 15%, (e) 30%. The right column contains (f) a cycled electrode for 1%FEC concentration followed by (g) 2%, (h) 5%, (i) 15%, and (j) 30%

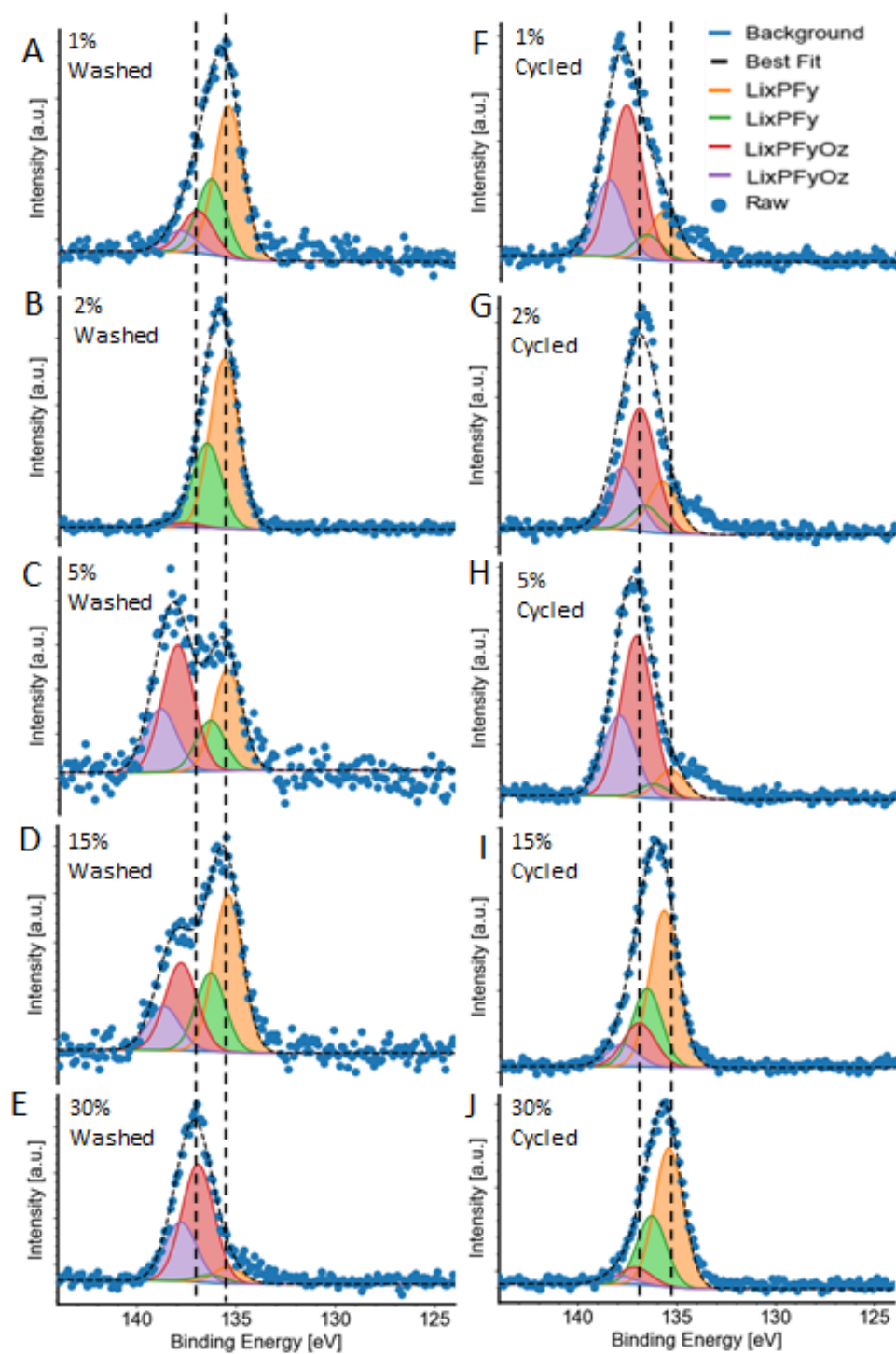


Figure 4.9 XPS spectra of P 2p core level gathered from 143-124 eV plotted on individual y-scales. (a) is a washed electrode with 1% FEC concentration with LixPFy peak doublet in orange and green, LixPFyOz peak doublet in red and purple, and Liw-uPFz-v is the same for all panels. (b) 2% FEC concentration, (c) 5% (d) 15%, (e) 30%. The right column contains (f) a cycled electrode for 1%FEC concentration followed by (g) 2%, (h) 5%, (i) 15%, and (j) 30%

ratio of C-F to total carbon content is linear. In panel A the concentration of C-F bonds to C-C bonds has a peak for the washed electrodes at 15% whereas the cycled electrodes have the largest C-F concentration at 2%. When comparing to panel B the C-F concentration as a function of the total C 1s area is more linear and consistent for both test cases. This implies that the amount of conductive carbon and contaminants on the surface of the electrodes could vary between cells. Assuming the electrodes are uniform then also implies that the conductive carbon is reacting with Li<sup>+</sup> ions and further contributing to the degradation of the electrolyte by pulling the free Li out of the electrolyte solution. The other carbon species present in the C 1s spectrum are attributed to residual solvent, various surface carbonates, and hydro-carbonates. Careful analysis of the P 2p spectrum reveals drastic chemical and electronic changes of the PF<sub>6</sub> ion due to the Li<sub>x</sub>PF<sub>y</sub> species found on the NMC cathode. From Figure 4.8 we argue that the total concentration of PvdF in these electrodes does not vary intensely as the constant concentration of C-F bond in the C 1s spectrum is associated only with PvdF. The appearance of Li<sub>x</sub>PF<sub>y</sub>O<sub>z</sub> is also likely in Figure 4.9 and Figure 4.10 for FEC concentrations 5% and up.

Figure 4.10 shows the XPS results for the O1s core level. The orange peak near 532.5 eV and the green peak near 534.5 eV are assigned to Li<sub>2</sub>CO<sub>3</sub> and other carbonate contamination [29], while the red peak at 531.7 eV is LiOH. In some panels the fourth purple peak at 528.9 eV appears representing the underlying cathode M-O material which essentially acts as the SEI sample substrate. The cycled electrodes show decreased amounts of Li<sub>2</sub>CO<sub>3</sub> at 532.5-532.9 eV with the washed electrode having a carbonate concentration that is about 15-25% higher for 1%, 2%, and 5% FEC concentration. The second carbonate peak at 534.2-534.6 eV shows the opposite trend with increased amounts of Li<sub>2</sub>CO<sub>3</sub>+ carbonates for 1%, 2%, and 5% FEC concentration. The Li<sub>2</sub>CO<sub>3</sub> concentration of the 15% and 30% samples were within 10%. The amount of LiOH increases substantially for 5%, 15% and 30% washed electrodes which widens and shifts the peak envelope of the O1s core level spectra. The M-O peak varies in intensity with FEC concentration. The 2%

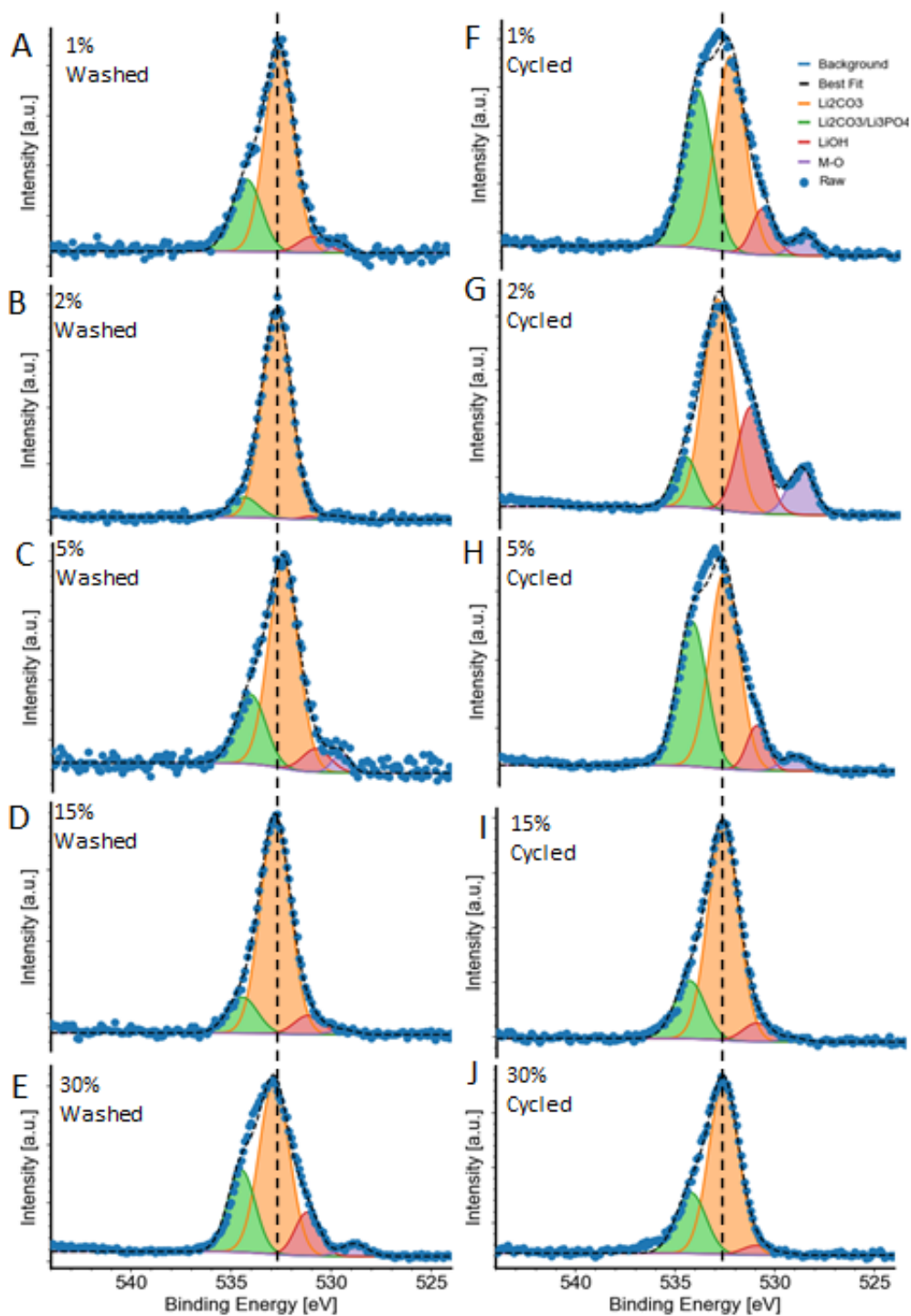


Figure 4.10 XPS spectra of O 1s core level gathered from 543-524eV plotted on individual y-scales. (a) is a washed electrode with 1% FEC concentration with  $\text{Li}_2\text{CO}_3$  peak in orange,  $\text{Li}_2\text{CO}_3/\text{Li}_x\text{PFyO}_z$  in green,  $\text{LiOH}$  in red, and M-O bond in purple as is the same for all panels. (b) 2% FEC concentration, (c) 5% (d) 15%, (e) 30%. The right column contains (f) a cycled electrode for 1%FEC concentration followed by (g) 2%, (h) 5%, (i) 15%, and (j) 30%

cycled electrode has the largest M-O peak along with a large amount of broadening and centroid shift of the  $\text{Li}_2\text{CO}_3$  peak. Indeed in all spectra a connection between the intensity of the M-O peak and the peak shape, size, and position of the  $\text{Li}_2\text{CO}_3$  and any emergence of phosphate species.

Table 4.3 Washed and Cycled electrode XPS core level peak area ratios. Percent form for Gen 2 and each FEC concentration 0%, 1%, 2%, 5%, 15%, and 30% broken between  $\text{LiF}$  and  $\text{Li}_y\text{PF}_x+\text{PvDF}$  components for F 1s, O-C-O, C-O, H-C-O, and C-F components for C 1s,  $\text{Li}_x\text{PyF}_z$  and  $\text{PvDF}$  for P2p, and  $\text{Li}_2\text{CO}_3$ ,  $\text{LiOH}$ , and M-O for O 1s.

Sample	Peak Assignment	Gen 2	1%	2%	5%	15%	30%
F 1s Washed	LiF	15.5	10.7	21.4	23.4	34.2	42.1
	$\text{PF}_x+\text{PvDF}$	82.6	86.8	79.2	75.3	67.3	56.6
Cycled	LiF	N/A	35.2	16.9	33.1	33.7	38.9
	$\text{PF}_x+\text{PvDF}$	N/A	61.0	83.4	66.0	64.9	60.0
C 1s Washed	C-C	58.6	60.0	59.3	59.7	60.3	47.2
	C-H	4.5	5.0	5.0	5.7	5.9	9.9
	C-O	17.8	17.3	17.7	16.7	15.9	20.6
	C=O	3.4	3.4	3.4	3.5	3.8	9.8
	C-F	12.8	12.3	12.4	11.6	11.2	9.8
Cycled	C-C	N/A	51.3	51.0	50.4	57.9	53.7
	C-H	N/A	6.5	5.9	7.3	5.2	6.7
	C-O	N/A	20.3	21.8	20.0	18.2	19.8
	C=O	N/A	7.3	7.2	8.9	4.3	4.9
	C-F	N/A	11.4	9.9	10.4	12.0	12.2
P 2p Washed	$\text{Li}_x\text{PF}_y$	88.9	67.2	93.2	44.7	59.1	9.9
	$\text{Li}_x\text{PyFO}_z$	8.6	20.1	2.8	61.4	36.2	78.4
Cycled	$\text{Li}_x\text{PF}_y$	N/A	21.3	25.4	12.4	72.1	76.9
	$\text{Li}_x\text{PyFO}_z$	N/A	71.3	66.0	76.3	22.0	10.4
O 1s Washed	$\text{Li}_2\text{CO}_3$	78.9	65.9	87.9	64.5	76.0	56.8
	$\text{Li}_2\text{CO}_3+\text{cont.}$	12.9	24.4	8.3	21.8	12.7	24.9
	LiOH	0.2	3.7	0.7	6.8	6.2	11.6
	M-O	2.7	2.2	1.4	3.5	1.4	3.6
Cycled	$\text{Li}_2\text{CO}_3$	N/A	46.6	39.5	50.0	71.7	66.7
	$\text{Li}_2\text{CO}_3+\text{cont.}$	N/A	37.7	42.6	36.9	19.2	23.4
	LiOH	N/A	8.4	5.8	7.8	5.8	3.5
	M-O	N/A	4.0	8.6	3.3	0.9	0.0

Table 4.3 records the relative peak area intensity ratios to the total raw area of each corresponding core level. Indeed  $\text{LiF}$  concentration increases with FEC loading in the F 1s

spectra for the washed electrodes while the binder peak decreases. The F 1s spectra of the cycled electrodes shows a similar trend for LiF accumulation except for 1% loading which surprisingly has the second largest ratio for LiF. The C 1s core level shows a consistent amount of C-C portion of the carbon binder material with the C-F bond of the PvDF binding material decreasing with FEC loading for washed electrodes. Moreover the O-C-O bond steadily rises with FEC loading. The C 1s scans of the cycled electrodes show the same trend for the C-C bond but unlike the washed electrodes shows an increase in the C-F concentration if 1% FEC loading is ignored. The O 1s core level scans show the characteristic  $\text{Li}_2\text{CO}_3$  peak at 532.5 eV. For the cycled electrodes the intensity of the carbonate peak directly increases with FEC concentration while the secondary carbonate peak at 534.4 eV decreases. Furthermore, the M-O peak at 528.9 eV only appears for FEC loadings under 5% for the cycled electrodes while appearing for only 30% FEC in the washed electrodes.

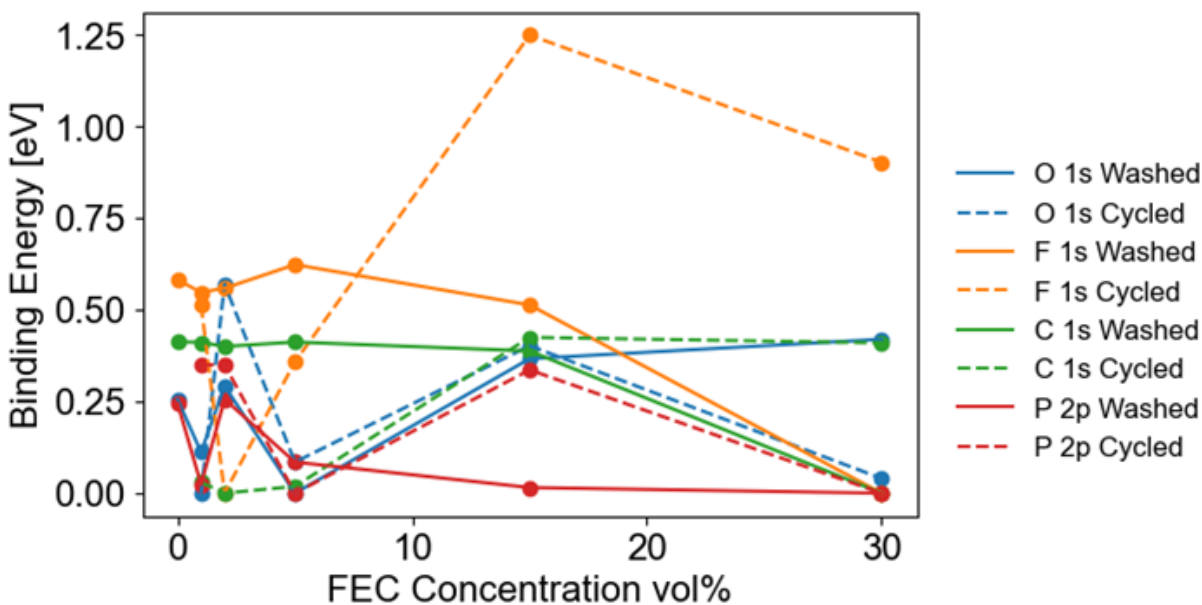


Figure 4.11 XPS centroid shifts plotted for 1%, 2%, 5%, 15%, and 30% FEC concentrations for both washed solid line and cycled electrodes dashed line. Centroids are plotted for F 1s, C 1s, O 1s, and P 2p core levels.

## 4.3 Discussion

### 4.3.1 FEC Effects on Electrochemical Performance

The characterization of the electrodes from the devices used in this study provides useful insights into the cause of the capacity drop of FEC containing cells after the initial discharge cycles. The voltage decay seen in Figure 4.1 trends upwards with FEC concentration implying that the kinetic losses of  $\text{Li}^+$  increase with available fluorine content due to the donation of F ions in the electrolyte [16]. The discharge capacity plots support the claim of kinetic losses of  $\text{Li}^+$  as each FEC concentration has a sharp decrease above 4.0 V. The Warburg impedance seen in Figure 4.2 and calculated in Table 4.1 also indicates kinetic losses of  $\text{Li}^+$  that are due to the increased Nernst diffusion length used in 3.4 to determine the Warburg coefficient. Moreover, the broad capacity loss seen in Figure 4.1 suggests that the diffusion coefficient of Li in the electrolyte decreases with FEC content as has been shown in other studies [7, 8, 19]. Concurrently FEC has also been shown to improve Li transport through the SEI [41]. Zhou et al. propose that the optimal percentage of 5% FEC promotes the charge transfer of  $\text{Li}^+$  while decreasing electrolyte decomposition [48]. Comparing the second semi-circles in Figure 4.2 does show that the 5% FEC loading has a smaller charge transfer resistance than the other concentrations except for 30%. Moreover, the 5% and 30% EIS curves indicate a thicker SEI with the increases SEI resistance shown by the first semi-circles. In Figure 4.1 the 5% FEC was the only cell to experience dramatic capacity and voltage loss after the second discharge cycle which suggests that 5% FEC loading may not be the optimal concentration for NMC/graphite full cells. The linear portion of the discharge capacity curves between 3.4 V and 3.7 volts have a similar slope, but the linear portion between 3.7 V and 4.0V vary greatly between FEC concentrations with no apparent trend. The change of slope in this region can be attributed to resistance changes in the cells that can occur from the accumulation of inorganic species on the electrodes [41]. The final portion of the discharge capacity curve in Figure 4.1 for 1%, 2% and 5% FEC is steeper than the 15% and 30% curve for both set of

cells. This implies that Li diffusion through the SEI and into the cathode is promoted between 1%-5% FEC concentration [41].

The SEI resistance and capacitance of the cells along with the charge transfer resistance and Warburg impedance can be used to quantify the effects of FEC on full cell performance. Fernandez et al. argue that changes in Ohmic resistance represent the decomposition of the binder material, while the SEI resistance, capacitance, and charge transfer resistance are affected by the build-up of the SEI, particle cracking, and Li plating [42]. The primary changes in the impedance spectra for this study can be explained solely by the effects of FEC as all other variables remain constant. Moreover, as presented in Chapter 2 FEC primarily affects cell performance through the formation of a LiF rich SEI. Therefore, important results like the SEI thickness, Li conductivity through the SEI, and charge transfer rate can be supported by the EIS spectra and connected to FEC concentration. The exchange current density described by 3.3 provides insight into the charge transfer resistance and subsequent shape of the second EIS semi-circle in Figure 4.2. Figure 4.2 in conjunction with 3.3 suggests that the increase in available F ions by the addition of FEC increases the concentration of reductive species at the NMC surface. This accumulation of F ions is what ultimately promotes the formation of LiF and is the most likely cause of the extended diameters causing elongated semi-circles in the EIS spectra. Regrettably, the noise prevalent in the EIS instrumentation trivializes the comparison of the Ohmic resistance of the cells.

### **4.3.2 Surface Morphology and Structure of NMC Cathodes**

Another explanation for the decreased capacity is the pulverization of the NMC particles as seen in Figure 4.3. Although the pulverization is minor, SEM results suggest that increased loading of FEC reduces the mechanical degradation of NMC particles when comparing 2% and 15% to a pristine electrode, but overall particle cracking affects cannot be connected with FEC loadings in this study. However, other studies show that particle cracking of NMC, while minor below 4.2 V, may be improved by the addition of

fluorinated electrolyte additives like FEC [10, 23, 24]. Any capacity loss due to damage to the structure of the bulk material is unfounded by the similarities of the XRD spectra in Figure 4.4. Furthermore, no significant cation mixing was found in the NMC electrode when comparing the peak area intensities of the the 003 and 104 planes. Therefore, the crystalline structure of the NMC was stable during the initial discharge cycles, but the surface morphology was affected. The NMC particles appear to be less damaged at higher FEC loadings due to a thicker layer of the protective LiF-rich SEI.

### 4.3.3 Chemical State of the SEI and Polarizing Effects due to Electrolyte Decomposition

The difference in the XPS peak center shifts in Figure 4.11 for the O 1s and F 1s core levels is due to the appearance VC by the solvent decomposition of FEC [7]. Hekmatfar et al. showed that the thickness of the SEI layer decreases when VC is used as an additive compared to FEC. FEC and VC in combination alter the shape of the O 1s spectrum severely with the appearance of a carbonate peak near 535.4 eV and 292.5 eV. These peaks are not readily apparent in the C 1s spectrum Figure 4.8 of the cycled electrodes, but the O 1s spectrum Figure 4.10 suggests the appearance of polycarbonate species in 1%, 2%, and 5% FEC concentrations. Hekmatfar et al. also attributed any broadening in the  $\text{Li}_x\text{PO}_y\text{F}_z$  peak assignment, similar to the green peak in Figure 4.7 to  $\text{Li}_x\text{PO}_y\text{F}_z$ . This plot shows that LiPF<sub>6</sub> degrades when in contact with an NMC electrode. The decomposition products then form Li<sub>2</sub>CO<sub>3</sub>, LiOH, in the presence of air. Moreover, the PF<sub>6</sub><sup>-</sup> ion becomes defluorinated into PF<sub>6-x</sub> contributing to the formation of LiF. The change in size between the C-O, C=O, and COOR peaks in Figure 4.8 can also be explained by the reduction of FEC into VC at higher additive concentrations [7]. However, the graphitic content of these electrodes reacts with the metal oxides or Li carbonates to form C-O bonds that reduce the conductivity of the electrodes. These reactions seem to occur faster with increased FEC concentration implying that the decomposition of FEC is the preferred reaction once enough additive is present.

To model effect of electrolyte decomposition and the parasitic reactions at the cathode linear free energy relationship (LFER) studies have been performed on NMC containing LiBs [38]. Su et al. found no evidence correlating the solvation ability of the electrolyte with the decay of the LNMO cathode, but rather they found that a LFER exists between the solvation ability of the electrolyte and the parasitic reactions at the cathode. However, this solvation based decomposition does not appear to have a LFER under 4.4V cutoffs, so it cannot contribute to the performance loss at 4.2V. Instead, the anion salt degradation dominates capacity loss as well as the composition of the SEI [38]. A similar mechanism seems to affect the SEI composition shown in Figure 4.9.

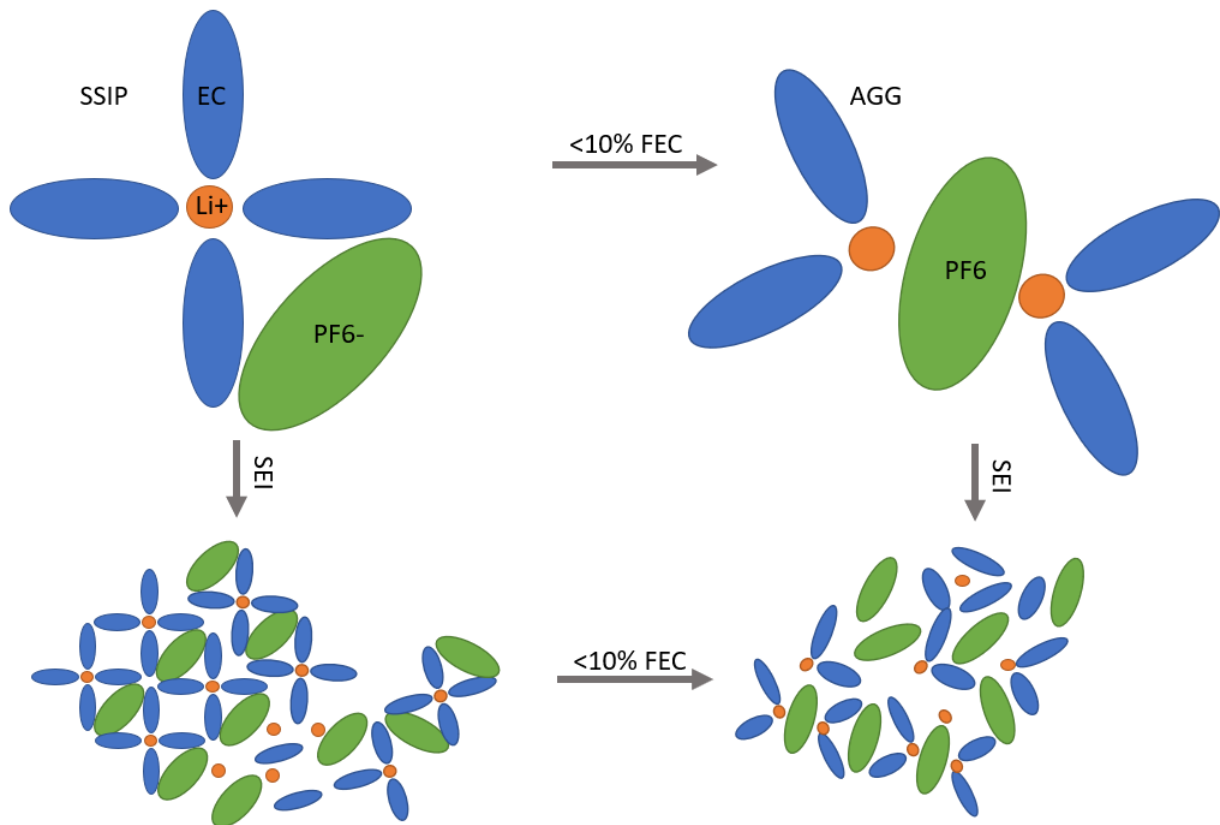


Figure 4.12 Schematic of the effect of FEC concentrations over 10% on solvation structure and SEI formation. EC is represented in blue shuttling orange Li ions in the SSIP configuration. The AGG configuration shows two Li cations and one PF6 anion along with the formation of the SEI.

Hou et al. simulated the effects of FEC concentration on the solvation structure with molecular dynamics and quantum chemical calculations. They found that 10% FEC concentration modifies the Li solvation structure by increasing the contact-ion pair ratio when compared to standard EC electrolytes [25]. A change from the SSIP to AGG solvation structures is depicted in Figure 4.12 along with the resulting SEI chemistry. For FEC concentrations over 5% the SEI shows more  $\text{Li}_x\text{PyFz}$  species as shown in Table 4.3. Moreover they attribute any polarization affects to this increase in contact-ion pairs which allows more Li ions to interact with PF species causing the reduction potentials of the electrolyte to change [25]. The more interaction means the more reaction and decomposition of the electrolyte resulting in the formation of a thicker SEI which shows a polarizing affect in the XPS data due to the accumulation of Li.

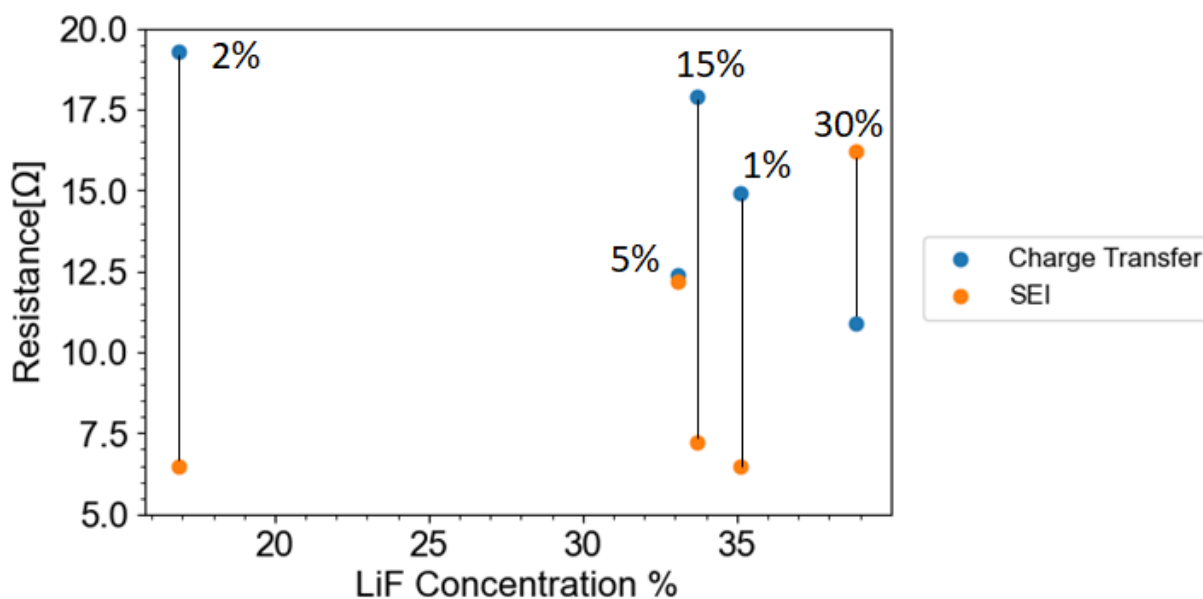


Figure 4.13 Resistance  $\Omega$  versus LiF concentration using the peak area ratio of the LiF peak assignment in the XPS F 1s core level. Charge transfer resistance is displayed in blue and SEI resistance in orange. FEC concentrations are included as figure labels. Black lines pair the data sets and indicate differences in the resistance values

Figure 4.13 summarizes the lack of connection between LiF concentration and component resistances gathered from EIS results. The charge transfer resistance for each

FEC concentration is greater than the SEI contribution except for 30% FEC. The 2% shows the widest range between SEI and charge transfer resistance implying a thinner SEI layer was formed at the anode while the increased charge transfer resistance effects indicate a thicker CEI layer. The 5% FEC has an overlap of resistances which implies a similar SEI thickness assuming the increase is mainly due to the accumulation of LiF. However, LiF concentration appears to have no connection to FEC loading during cycling except for the fact that the 2% FEC concentration showed similar resistances to the 30% FEC with a difference in LiF concentration of 20%. One explanation for these results is the formation of a SEI layer with varying composition over 5% FEC due to the change oxidation products of the electrolyte and abundance of F ions [25] .

## CHAPTER 5

### CONCLUSION

#### 5.1 General Summary

To help solve the challenges associated with energy storage the effects of the electrolyte additive FEC on NMC cathodes and cell performance were investigated. Specifically the effects of FEC on electrolyte decomposition and the resulting chemistry of the CEI were characterized using EIS, XPS, XRD, and SEM. Results from the literature in chapter 2 show FEC as a promising electrolyte additive for several reasons. One, FEC has good chemical stability with many electrode materials including Li metal, Li-S, and NMC. Two, FEC is stable with carbonate based electrolytes. And three, FEC extends the lifetimes of Li-ion batteries. Two primary decomposition modes of FEC are also reported. The first is the electrolyte salt anion decomposition and the second is the electrolyte solvent reduction reaction. Both reactions contribute to the composition of the SEI and both result in the formation of LiF, but the overall chemistry changes along with LiF concentration.

The basic principles of EIS, XPS, XRD, and SEM were summarized and their application to this study explained in chapter 3. EIS provided insight into the electrochemical performance and SEI characteristics of the fabricated devices. XPS was used to examine the chemical state of the SEI; while SEM and XRD were used to monitor the electrode surface morphology and crystallographic structure. While the electrodes used in this study were purchased off the shelf, electrode fabrication and device assembly was also detailed for reference. In chapter 4 the results from the above techniques are used to determine the effects of FEC as an electrolyte additive. Morphological and crystallographic data from SEM and XRD showed minimal connection with FEC concentration. The XRD spectra did show minor cation mixing for concentrations over 5% FEC, but over all crystallographic structure did not change with FEC loading. Some particle cracking was

observed in the cycled electrodes, but this is attributed to the 4.2 V voltage limit during cycling. EIS and XPS suggest the successful use of FEC as an electrolyte additive to promote the thin film formation of LiF has demonstrated the ability to engineer the CEI. The method is both economical and promotes the chemical stability of the cathode surface. Recent studies show that higher concentrations of FEC act as a co-solvent [21] and no longer have the same properties as lower FEC concentrations [27]. This study has provided insight into the mechanism at which LiF is formed on NMC cathodes, and how the addition of FEC at the optimal concentration can stabilize the initial charge transfer resistance. Furthermore, the formation of LiF on the cathode surface has been shown to have a polarizing effect [27] that can be observed and quantified using XPS peak shifts.

## 5.2 Outlook

Future work in the context of this study would be the careful examination of the transition metals in the NMC cathode using XPS. The relevant Ni, Mn, and Co core levels need to be measured to determine the chemical state of the interface between the cathode and SEI. The Ni concentration and identity of the Ni chemical state would provide necessary insight into the affects of FEC on Ni dissolution. Similarly, Mn and Co core levels should be measured to further investigate transition metal dissolution. Moreover, the Li 1s core level must be measured and peak deconvolution performed between the Li species and the overlapping Mn 3s core level. This would give more insight into the formation of LiF,  $\text{Li}_x\text{PF}_y$ , and  $\text{Li}_x\text{PF}_y\text{O}_z$  and the corresponding electrolyte decomposition mechanisms.

The FEC concentration at which electrolyte solvent decomposition could also be an important avenue of new research. The literature review in chapter 2 has shown conflicting optimal concentrations of FEC additive for different electrode materials as well as different device capacities i.e. coin and pouch cells, vs 18650 cylindrical cells. The preferred mechanisms behind Li transport and SEI formation seem to change with FEC concentration but this connection is not yet well modeled or empirically understood. A study on the effects of FEC concentration ranging from 10%-15% vol. in a small

NMC/graphite system may hold the key to understanding the tipping point between salt anion decomposition and electrolyte reduction. Similarly, a study investigating the chemical changes in the electrolyte solution during cycling could determine which degradation route is more likely and subsequently which reaction dominates the composition of the SEI.

The examination and characterization of NMC electrodes at different stages of device life would demonstrate any changes in the SEI composition from what is reported in this study after the end of the initial discharge cycles. These results would provide insight into the continuous decomposition of the electrolyte and the corresponding effects on SEI composition. Furthermore, the reversibility of the SEI components, including,  $\text{Li}_x\text{PF}_y$ , and  $\text{Li}_x\text{PF}_y\text{O}_z$  could be examined in greater depth. The effects of FEC on fast charging scenarios would be another valuable study. The optimal FEC concentration could be chosen as an additive to several cells that are cycled at increased voltage limits and charge rates. The data provided in this study provides a baseline chemistry for the SEI that could be used in comparison to determine any composition changes that can be solely attributed to the device cycling conditions.

## REFERENCES

- [1] Tianyu Li, Xiao-Zi Yuan, Lei Zhang, Datong Song, Kaiyuan Shi, and Christina Bock. Degradation mechanisms and mitigation strategies of nickel-rich nmc-based lithium-ion batteries. *Electrochemical Energy Reviews*, 3(1):43–80, Mar 2020. ISSN 2520-8136. doi: 10.1007/s41918-019-00053-3.
- [2] Hardik Keshan, Jesse Thornburg, and Taha Selim Ustun. Comparison of lead-acid and lithium ion batteries for stationary storage in off-grid energy systems. In *4th IET Clean Energy and Technology Conference (CEAT 2016)*, pages 1–7, 2016. doi: 10.1049/cp.2016.1287.
- [3] Abraham Alem Kebede, Thierry Coosemans, Maarten Messagie, Towfik Jemal, Henok Ayele Behabtu, Joeri Van Mierlo, and Maitane Berecibar. Techno-economic analysis of lithium-ion and lead-acid batteries in stationary energy storage application. *Journal of Energy Storage*, 40:102748, 2021. ISSN 2352-152X. doi: <https://doi.org/10.1016/j.est.2021.102748>.
- [4] Kjell Schroder, Judith Alvarado, Thomas A. Yersak, Juchuan Li, Nancy Dudney, Lauren J. Webb, Ying Shirley Meng, and Keith J. Stevenson. The effect of fluoroethylene carbonate as an additive on the solid electrolyte interphase on silicon lithium-ion electrodes. *Chemistry of Materials*, 27(16):5531–5542, Aug 2015. ISSN 0897-4756. doi: 10.1021/acs.chemmater.5b01627.
- [5] Liumin Suo, Weijiang Xue, Mallory Gobet, Steve G. Greenbaum, Chao Wang, Yuming Chen, Wanlu Yang, Yangxing Li, and Ju Li. Fluorine-donating electrolytes enable highly reversible 5-v-class li metal batteries. *Proceedings of the National Academy of Sciences*, 115(6):1156–1161, Feb 2018. ISSN 0027-8424, 1091-6490. doi: 10.1073/pnas.1712895115.
- [6] Hieu Quang Pham, Marta Mirolo, Mohamed Tarik, Mario El Kazzi, and Sigita Trabesinger. Multifunctional electrolyte additive for improved interfacial stability in ni-rich layered oxide full-cells. 33:216–229, Dec 2020. ISSN 2405-8297. doi: 10.1016/j.ensm.2020.08.026.
- [7] Maral Hekmatfar, Ivana Hasa, Ramtin Eghbal, Diogo V. Carvalho, Arianna Moretti, and Stefano Passerini. Effect of electrolyte additives on the LiNi<sub>0.5</sub>Mn<sub>0.3</sub>Co<sub>0.2</sub>O<sub>2</sub> surface film formation with lithium and graphite negative electrodes. 7(1):1901500. ISSN 2196-7350. doi: 10.1002/admi.201901500. URL <https://onlinelibrary.wiley.com/doi/abs/10.1002/admi.201901500>. eprint: <https://onlinelibrary.wiley.com/doi/pdf/10.1002/admi.201901500>.

- [8] Anulekha K. Haridas, Quan Anh Nguyen, Tanguy Terlier, Rachel Blaser, and Sibani Lisa Biswal. Investigating the compatibility of TTMSF and FEC electrolyte additives for  $\text{LiNi}_{0.5}\text{Mn}_{0.3}\text{Co}_{0.2}\text{O}_2$  (NMC)-silicon lithium-ion batteries. 13(2): 2662–2673. ISSN 1944-8252. doi: 10.1021/acsami.0c19347.
- [9] Dong Ren, Yun Shen, Yao Yang, Luxi Shen, Barnaby D.A. Levin, Yingchao Yu, David A. Muller, and Héctor D. Abruña. Systematic optimization of battery materials: Key parameter optimization for the scalable synthesis of uniform, high-energy, and high stability  $\text{LiNi}_{0.6}\text{Mn}_{0.2}\text{Co}_{0.2}\text{O}_2$  cathode material for lithium-ion batteries. *ACS Applied Materials Interfaces*, 9(41):35811–35819, Oct 2017. ISSN 1944-8244. doi: 10.1021/acsami.7b10155.
- [10] Wangda Li, Xiaoming Liu, Qiang Xie, Ya You, Miaofang Chi, and Arumugam Manthiram. Long-term cyclability of ncm-811 at high voltages in lithium-ion batteries: an in-depth diagnostic study. *Chemistry of Materials*, 32(18):7796–7804, Sep 2020. ISSN 0897-4756, 1520-5002. doi: 10.1021/acs.chemmater.0c02398.
- [11] Seong-Jin Park, Jang-Yeon Hwang, Chong S. Yoon, Hun-Gi Jung, and Yang-Kook Sun. Stabilization of lithium-metal batteries based on the in situ formation of a stable solid electrolyte interphase layer. *ACS Applied Materials Interfaces*, 10(21): 17985–17993, May 2018. ISSN 1944-8244. doi: 10.1021/acsami.8b04592.
- [12] Pengfei Yan, Jianming Zheng, Jian Liu, Biqiong Wang, Xiaopeng Cheng, Yuefei Zhang, Xueliang Sun, Chongmin Wang, and Ji-Guang Zhang. Tailoring grain boundary structures and chemistry of ni-rich layered cathodes for enhanced cycle stability of lithium-ion batteries. *Nature Energy*, 3(7):600–605, Jul 2018. ISSN 2058-7546. doi: 10.1038/s41560-018-0191-3.
- [13] Zhiqiang Zhu, Yuxin Tang, Zhisheng Lv, Jiaqi Wei, Yanyan Zhang, Renheng Wang, Wei Zhang, Huarong Xia, Mingzheng Ge, and Xiaodong Chen. Fluoroethylene carbonate enabling a robust lif-rich solid electrolyte interphase to enhance the stability of the  $\text{MoS}_2$  anode for lithium-ion storage. *Angewandte Chemie International Edition*, 57(14):3656–3660, 2018. ISSN 1521-3773. doi: 10.1002/anie.201712907.
- [14] R. Genieser, S. Ferrari, M. Loveridge, S. D. Beattie, R. Beanland, H. Amari, G. West, and R. Bhagat. Lithium ion batteries (NMC/graphite) cycling at 80 °c: Different electrolytes and related degradation mechanism. 373:172–183. ISSN 0378-7753. doi: 10.1016/j.jpowsour.2017.11.014. URL <https://www.sciencedirect.com/science/article/pii/S0378775317314738>.

- [15] Aurélie Guéguen, Daniel Streich, Minglong He, Manuel Mendez, Frederick F. Chesneau, Petr Novák, and Erik J. Berg. Decomposition of LiPF<sub>6</sub> in high energy lithium-ion batteries studied with online electrochemical mass spectrometry. 163(6): A1095. ISSN 1945-7111. doi: 10.1149/2.0981606jes. URL <https://iopscience.iop.org/article/10.1149/2.0981606jes/meta>. Publisher: IOP Publishing.
- [16] Liumin Suo, Weijiang Xue, Mallory Gobet, Steve G. Greenbaum, Chao Wang, Yuming Chen, Wanlu Yang, Yangxing Li, and Ju Li. Fluorine-donating electrolytes enable highly reversible 5-v-class li metal batteries. 115(6):1156–1161. ISSN 0027-8424, 1091-6490. doi: 10.1073/pnas.1712895115. URL <http://www.pnas.org/lookup/doi/10.1073/pnas.1712895115>.
- [17] Fluoroethylene carbonate as electrolyte additive for improving the electrochemical performances of high-capacity li<sub>1.16</sub>[mn<sub>0.75</sub>ni<sub>0.25</sub>]o<sub>0.84</sub>o<sub>2</sub> material. 168. ISSN 0013-4686. doi: 10.1016/j.electacta.2015.04.030.
- [18] J. Lee, Y.-J. Kim, H.S. Jin, H. Noh, H. Kwack, H. Chu, F. Ye, H. Lee, and H.-T. Kim. Tuning two interfaces with fluoroethylene carbonate electrolytes for high-performance li/LCO batteries. 4(2):3220–3227. ISSN 2470-1343. doi: 10.1021/acsomega.8b03022.
- [19] H. Zhou, B. Liu, D. Xiao, C. Yin, and J. Li. Fluoroethylene carbonate as the additive of lithium difluoro(oxalate)borate–sulfolane electrolytes to improve the electrochemical performance of LiNi<sub>0.5</sub>mn<sub>1.5</sub>o<sub>4</sub> cathode. 30(5):5098–5108. ISSN 0957-4522. doi: 10.1007/s10854-019-00808-0.
- [20] Ortal Lavi, Shalom Luski, Netanel Shpigel, Chen Menachem, Zvika Pomerantz, Yuval Elias, and Doron Aurbach. Electrolyte solutions for rechargeable li-ion batteries based on fluorinated solvents. *ACS Applied Energy Materials*, 3(8):7485–7499, Aug 2020. ISSN 2574-0962, 2574-0962. doi: 10.1021/acsaem.0c00898.
- [21] Tingzheng Hou, Kara D. Fong, Jingyang Wang, and Kristin A. Persson. The solvation structure, transport properties and reduction behavior of carbonate-based electrolytes of lithium-ion batteries. *Chemical Science*, 12(44):14740–14751, 2021. doi: 10.1039/D1SC04265C.
- [22] J. Zhao, J. Wang, Z. Chang, and S. Lu. Performance of li-rich material with fluoroethylene carbonate as high-voltage electrolyte solvent. 42(10):1077–1083, . ISSN 0258-7076. doi: 10.13373/j.cnki.cjrm.XY17040007.


- [23] Yang Li, Fang Lian, Leilei Ma, Chunlan Liu, Lin Yang, Xiaomeng Sun, and Kuochih Chou. Fluoroethylene carbonate as electrolyte additive for improving the electrochemical performances of high-capacity  $\text{Li}_{1.16}[\text{Mn}_{0.75}\text{Ni}_{0.25}]_{0.84}\text{O}_2$  material. 168:261–270. ISSN 0013-4686. doi: 10.1016/j.electacta.2015.04.030. URL <https://www.sciencedirect.com/science/article/pii/S0013468615009081>.
- [24] S. Duangdangchote, N. Phattharasupakun, P. Chomkhuntod, P. Chiochan, S. Sarawutanukul, C. Tomon, N. Joraleechanchai, and M. Sawangphruk. Effect of fluoroethylene carbonate on the transport property of electrolytes towards ni-rich li-ion batteries with high safety. *Chemical Communications*, 57(55):6732–6735, 2021. ISSN 1359-7345. doi: 10.1039/d1cc02120f.
- [25] Tingzheng Hou, Guang Yang, Nav Nidhi Rajput, Julian Self, Sang-Won Park, Jagjit Nanda, and Kristin A. Persson. The influence of fec on the solvation structure and reduction reaction of  $\text{LiPF}_6/\text{EC}$  electrolytes and its implication for solid electrolyte interphase formation. *Nano Energy*, 64:103881, Oct 2019. ISSN 2211-2855. doi: 10.1016/j.nanoen.2019.103881.
- [26] Salatan Duangdangchote, Nutthaphon Phattharasupakun, Praeploy Chomkhuntod, Poramane Chiochan, Sangchai Sarawutanukul, Chanikarn Tomon, Nattanon Joraleechanchai, and Montree Sawangphruk. Effect of fluoroethylene carbonate on the transport property of electrolytes towards ni-rich li-ion batteries with high safety. 57 (55):6732–6735. ISSN 1364-548X. doi: 10.1039/D1CC02120F. URL <https://pubs.rsc.org/en/content/articlelanding/2021/cc/d1cc02120f>. Publisher: The Royal Society of Chemistry.
- [27] L. Liu, S. Wang, Z. Zhang, J. Fan, W. Qi, and S. Chen. Fluoroethylene carbonate as an electrolyte additive for improving interfacial stability of high-voltage  $\text{LiNi}_{0.6}\text{Co}_{0.2}\text{Mn}_{0.2}\text{O}_2$  cathode. 25(3):1035–1043. ISSN 0947-7047. doi: 10.1007/s11581-018-2641-0.
- [28] Jingteng Zhao, Xu Zhang, Yuan Liang, Zhijie Han, Shiqi Liu, Weiqin Chu, and Haijun Yu. Interphase engineering by electrolyte additives for lithium-rich layered oxides: Advances and perspectives. 6(7):2552–2564, . doi: 10.1021/acscenergylett.1c00750. URL <https://doi.org/10.1021/acscenergylett.1c00750>. Publisher: American Chemical Society.
- [29] P.G. Kitz, M.J. Lacey, P. Novak, and E.J. Berg. Operando investigation of the solid electrolyte interphase mechanical and transport properties formed from vinylene carbonate and fluoroethylene carbonate. *Journal of Power Sources*, 477, 2020. ISSN 0378-7753. doi: 10.1016/j.jpowsour.2020.228567.

- [30] Stabilization of lithium-metal batteries based on the in situ formation of a stable solid electrolyte interphase layer. 10. ISSN 1944-8244. doi: 10.1021/acsami.8b04592. URL <https://doi.org/10.1021/acsami.8b04592>.
- [31] Woon Ih Choi, Min Sik Park, Youngseon Shim, Dong Young Kim, Yoon-Sok Kang, Hyo Sug Lee, and Meiten Koh. Reductive reactions via excess li in mixture electrolytes of li ion batteries: an ab initio molecular dynamics study. 21(10): 5489–5498. ISSN 1463-9084. doi: 10.1039/C8CP04907F. URL <https://pubs.rsc.org/en/content/articlelanding/2019/cp/c8cp04907f>. Publisher: The Royal Society of Chemistry.
- [32] Roland Jung, Michael Metzger, Filippo Maglia, Christoph Stinner, and Hubert A. Gasteiger. Chemical versus electrochemical electrolyte oxidation on nmc111, nmc622, nmc811, Inmo, and conductive carbon. *The Journal of Physical Chemistry Letters*, 8 (19):4820–4825, Oct 2017. ISSN 1948-7185, 1948-7185. doi: 10.1021/acs.jpcclett.7b01927.
- [33] Vinodkumar Etacheri, Ortal Haik, Yossi Goffer, Gregory A. Roberts, Ionel C. Stefan, Rainier Fasching, and Doron Aurbach. Effect of fluoroethylene carbonate (fec) on the performance and surface chemistry of si-nanowire li-ion battery anodes. *Langmuir*, 28 (1):965–976, Jan 2012. ISSN 0743-7463. doi: 10.1021/la203712s.
- [34] Elena Markevich, Gregory Salitra, and Doron Aurbach. Fluoroethylene carbonate as an important component for the formation of an effective solid electrolyte interphase on anodes and cathodes for advanced li-ion batteries. *ACS Energy Letters*, 2(6): 1337–1345, Jun 2017. ISSN 2380-8195, 2380-8195. doi: 10.1021/acsenergylett.7b00163.
- [35] O. Tiurin, N. Solomatin, M. Auinat, and Y. Ein-Eli. Atomic layer deposition (ALD) of lithium fluoride (LiF) protective film on li-ion battery LiMn<sub>1.5</sub>Ni<sub>0.5</sub>O<sub>4</sub> cathode powder material. 448. ISSN 0378-7753. doi: 10.1016/j.jpowsour.2019.227373.
- [36] T. G. Stoebe and R. A. Huggins. Measurement of ionic diffusion in lithium fluoride by nuclear magnetic resonance techniques. *Journal of Materials Science*, 1(2):117–126, May 1966. ISSN 0022-2461, 1573-4803. doi: 10.1007/BF00550100.
- [37] Jiyu Cai, Han Gao, Guiliang Xu, Luxi Li, Yang Ren, Xiangbo Meng, Khalil Amine, and Zonghai Chen. Surface modification for suppressing interfacial parasitic reactions of nickel-rich lithium-ion cathode. *ECS Meeting Abstracts*, MA2019-01(2):306–306, May 2019. ISSN 2151-2043. doi: 10.1149/MA2019-01/2/306.

- [38] Chi-Cheung Su, Meinan He, Rachid Amine, Zonghai Chen, Zhou Yu, Tomas Rojas, Lei Cheng, Anh T. Ngo, and Khalil Amine. Unveiling decaying mechanism through quantitative structure-activity relationship in electrolytes for lithium-ion batteries. *Nano Energy*, 83:105843, May 2021. ISSN 2211-2855. doi: 10.1016/j.nanoen.2021.105843.
- [39] Antonin Grenier, Hao Liu, Kamila M. Wiaderek, Zachary W. Lebens-Higgins, Olaf J. Borkiewicz, Louis F. J. Piper, Peter J. Chupas, and Karena W. Chapman. Reaction heterogeneity in  $\text{LiNi}_{0.8}\text{Co}_{0.15}\text{Al}_{0.05}\text{O}_2$  induced by surface layer. 29(17):7345–7352. ISSN 0897-4756. doi: 10.1021/acs.chemmater.7b02236. URL <https://doi.org/10.1021/acs.chemmater.7b02236>. Publisher: American Chemical Society.
- [40] Tony Jaumann. Lifetime vs. rate capability: Understanding the role of fec and vc in high-energy li-ion batteries with nano-silicon anodes. *Energy Storage Materials*, 6: 26–35, Jan 2017. ISSN 2405-8297. doi: 10.1016/j.ensm.2016.08.002.
- [41] Anna B. Gunnarsdóttir, Sundeep Vema, Svetlana Menkin, Lauren E. Marbella, and Clare P. Grey. Investigating the effect of a fluoroethylene carbonate additive on lithium deposition and the solid electrolyte interphase in lithium metal batteries using in situ nmr spectroscopy. *Journal of Materials Chemistry A*, 8(30):14975–14992, Aug 2020. ISSN 2050-7496. doi: 10.1039/D0TA05652A.
- [42] Carlos Pastor-Fernández, W. Dhammika Widanage, James Marco, Miguel-Ángel Gama-Valdez, and Gael. H. Chouchelamane. Identification and quantification of ageing mechanisms in lithium-ion batteries using the eis technique. In *2016 IEEE Transportation Electrification Conference and Expo (ITEC)*, pages 1–6, 2016. doi: 10.1109/ITEC.2016.7520198.
- [43] Siegfried Hofmann. *Auger- and X-Ray Photoelectron Spectroscopy in Materials Science*, volume 49 of *Springer Series in Surface Sciences*. Springer, 2013. ISBN 978-3-642-27380-3. doi: 10.1007/978-3-642-27381-0. URL <http://link.springer.com/10.1007/978-3-642-27381-0>.
- [44] Oleksandr Bondarchuk, Alec P. LaGrow, Andriy Kvasha, Tho Thieu, Elixabete Ayerbe, and Idoia Urdampilleta. On the x-ray photoelectron spectroscopy analysis of  $\text{LiNi}_{0.8}\text{Mn}_{0.15}\text{Co}_{0.05}\text{O}_2$  material and electrodes. *Applied Surface Science*, 535:147699, Jan 2021. ISSN 0169-4332. doi: 10.1016/j.apsusc.2020.147699.
- [45] H. Stanjek and W. Häusler. Basics of x-ray diffraction. *Hyperfine Interactions*, 154(1): 107–119, Jun 2004. ISSN 1572-9540. doi: 10.1023/B:HYPE.0000032028.60546.38.

- [46] Nasrullah Khan, Saad Dilshad, Rashida Khalid, Ali Raza Kalair, and Naeem Abas. Review of energy storage and transportation of energy. 1(3):e49. ISSN 2578-4862. doi: 10.1002/est2.49. URL <https://onlinelibrary.wiley.com/doi/abs/10.1002/est2.49>. eprint: <https://onlinelibrary.wiley.com/doi/pdf/10.1002/est2.49>.
- [47] Antonin Grenier, Hao Liu, Kamila M. Wiaderek, Zachary W. Lebens-Higgins, Olaf J. Borkiewicz, Louis F. J. Piper, Peter J. Chupas, and Karena W. Chapman. Reaction heterogeneity in  $\text{LiNi}_{0.8}\text{Co}_{0.15}\text{Al}_{0.05}\text{O}_2$  induced by surface layer. *Chemistry of Materials*, 29(17):7345–7352, Sep 2017. ISSN 0897-4756. doi: 10.1021/acs.chemmater.7b02236.
- [48] Xuan Zhou, Ping Li, Zhihao Tang, Jialu Liu, Shaowei Zhang, Yingke Zhou, and Xiaohui Tian. Fec additive for improved sei film and electrochemical performance of the lithium primary battery. *Energies*, 14(2222):7467, Jan 2021. ISSN 1996-1073. doi: 10.3390/en14227467.

APPENDIX  
COPYRIGHT AND PERMISSIONS



**Long-Term Cyclability of NCM-811 at High Voltages in Lithium-Ion Batteries: an In-Depth Diagnostic Study**  
Author: Wangda Li, Xiaoming Liu, Qiang Xie, et al  
Publication: Chemistry of Materials  
Publisher: American Chemical Society  
Date: Sep 1, 2020  
*Copyright © 2020, American Chemical Society*

**PERMISSION/LICENSE IS GRANTED FOR YOUR ORDER AT NO CHARGE**

This type of permission/license, instead of the standard Terms and Conditions, is sent to you because no fee is being charged for your order. Please note the following:

- Permission is granted for your request in both print and electronic formats, and translations.
- If figures and/or tables were requested, they may be adapted or used in part.
- Please print this page for your records and send a copy of it to your publisher/graduate school.
- Appropriate credit for the requested material should be given as follows: "Reprinted (adapted) with permission from (COMPLETE REFERENCE CITATION). Copyright (YEAR) American Chemical Society." Insert appropriate information in place of the capitalized words.
- One-time permission is granted only for the use specified in your RightsLink request. No additional uses are granted (such as derivative works or other editions). For any uses, please submit a new request.

If credit is given to another source for the material you requested from RightsLink, permission must be obtained from that source.

[BACK](#) [CLOSE WINDOW](#)

Figure A.1 Copyright permission for Figure 2.1, Figure 2.2, and Figure 2.4

**Stabilization of Lithium-Metal Batteries Based on the in Situ Formation of a Stable Solid Electrolyte Interphase Layer**

 **Author:** Seong-jin Park, Jang-Yeon Hwang, Chong S. Yoon, et al  
**Publication:** Applied Materials  
**Publisher:** American Chemical Society  
**Date:** May 1, 2018  
*Copyright © 2018, American Chemical Society*

**PERMISSION/LICENSE IS GRANTED FOR YOUR ORDER AT NO CHARGE**

This type of permission/license, instead of the standard Terms and Conditions, is sent to you because no fee is being charged for your order. Please note the following:


- Permission is granted for your request in both print and electronic formats, and translations.
- If figures and/or tables were requested, they may be adapted or used in part.
- Please print this page for your records and send a copy of it to your publisher/graduate school.
- Appropriate credit for the requested material should be given as follows: "Reprinted (adapted) with permission from {COMPLETE REFERENCE CITATION}. Copyright {YEAR} American Chemical Society." Insert appropriate information in place of the capitalized words.
- One-time permission is granted only for the use specified in your RightsLink request. No additional uses are granted (such as derivative works or other editions). For any uses, please submit a new request.

If credit is given to another source for the material you requested from RightsLink, permission must be obtained from that source.

[BACK](#) [CLOSE WINDOW](#)

Figure A.2 Copyright permission for Li dead layer shown in Figure 2.3

**Effect of Fluoroethylene Carbonate (FEC) on the Performance and Surface Chemistry of Si-Nanowire Li-Ion Battery Anodes**

 **Author:** Vinodkumar Etacheri, Ortal Haik, Yossi Goffer, et al  
**Publication:** Langmuir  
**Publisher:** American Chemical Society  
**Date:** Jan 1, 2012  
*Copyright © 2012, American Chemical Society*

**PERMISSION/LICENSE IS GRANTED FOR YOUR ORDER AT NO CHARGE**

This type of permission/license, instead of the standard Terms and Conditions, is sent to you because no fee is being charged for your order. Please note the following:

- Permission is granted for your request in both print and electronic formats, and translations.
- If figures and/or tables were requested, they may be adapted or used in part.
- Please print this page for your records and send a copy of it to your publisher/graduate school.
- Appropriate credit for the requested material should be given as follows: "Reprinted (adapted) with permission from {COMPLETE REFERENCE CITATION}. Copyright {YEAR} American Chemical Society." Insert appropriate information in place of the capitalized words.
- One-time permission is granted only for the use specified in your RightsLink request. No additional uses are granted (such as derivative works or other editions). For any uses, please submit a new request.

If credit is given to another source for the material you requested from RightsLink, permission must be obtained from that source.

Figure A.3 Copyright permission for FEC decomposition schematic Figure 2.5

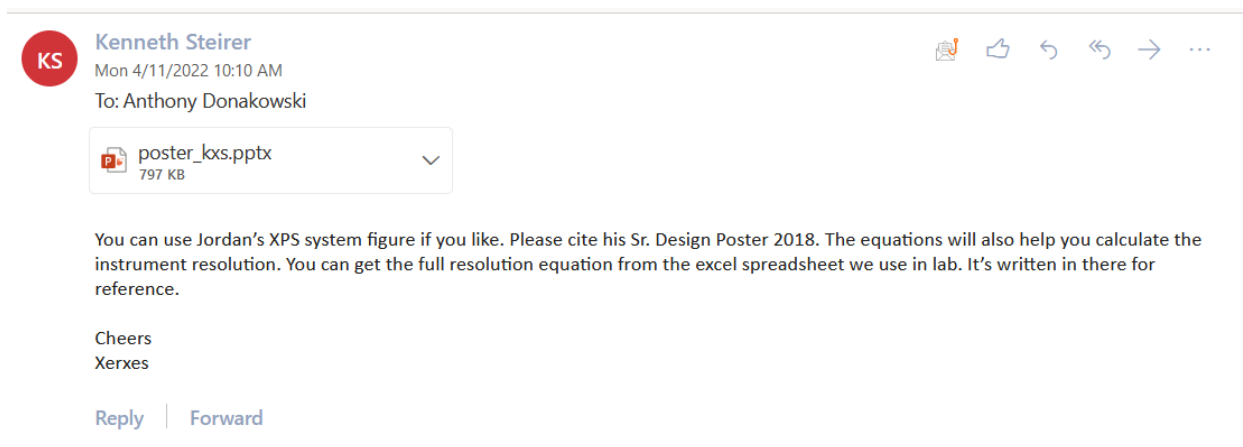


Figure A.4 Copyright permission for XPS schematic in Figure 3.4